

A hybrid FTIR and dispersive spectrometer: walk-through an optimized design

by

Federico Davoli

Submitted to the Department of Electronics Engineering
on March 25, 2016, in partial fulfillment of the
requirements for the degree of
Master of Science in Electronics Engineering

Abstract

Spectroscopy is a widely spread technique to identify chemical compounds in many areas, from biomedical to military applications. Two main types of spectrometers are available, Fourier Transform Spectrometers and Dispersive Spectrometers; while the first one records the self interference of the incoming signal, the second one uses a diffraction grating to disperse the incoming light on a CCD array. Advantages of the FTIR spectrometers are resolution and speed, however they are susceptible to fluorescence noise, reason why they should operate with IR excitation wavelengths. On the other side dispersive spectrometers are limited in resolution by the CCD array, but they can operate at higher wavelengths, hence obtaining a better signal to noise ratio. In this thesis a hybrid spectrometer that tries to combine the advantages of both technologies is designed. The dispersive section has been simulated, accounting all possible sources of optical aberration and signal degradation, and the interferometer section has been built and tested, with a particular care on the moving mirror dynamics. Various drives were explored, to find the one that better fits our design.

Thesis Supervisor: Meriç Özcan

Title: Associate Professor, Department of Electronics Engineering,
Sabanci University

A hybrid FTIR and dispersive spectrometer: walk-through an optimized design

by

Federico Davoli

Submitted to the Department of Electronics Engineering
on March 25, 2016, in partial fulfillment of the
requirements for the degree of
Master of Science in Electronics Engineering

Abstract

Spektroskopi biyomedikal alanlardan askeri uygulamalara kadar birçok alanda kimyasal bileşenleri tanımlamak üzere geniş çapta kullanılan bir tekniktir. Fourier Dönüşüm (FTIR) ve Dağıtıcı spektrometre olmak üzere iki farklı spektrometre bulunmaktadır. Fourier Dönüşümü spektrometresi gelen sinyalin kendi girişimini kayıt etmede kullanılırken Dağıtıcı spektrometre gelen ışığı CCD düzlemine dağıtmak için dağıtıcı ızgarası (diffraction grating) kullanmaktadır. FTIR spektrometrelerinin avantajı çözünürlüğün yüksek ve hızlarının fazla olması iken flüorışma (fluorescence) gürültü süne duyarlı olmaları spektrometrelerin kızılötesi uyarım dalgaboylarında çalışmalarına neden olmaktadır. Dağıtıcı spektrometreler CCD düzlem dolayısı ile sınırlı çözünürlüğe sahip olmakta fakat daha yüksek dalgaboylarında çalışabilmektedirler. Bu durum daha iyi bir sinyal gürültü oranı elde edilmesini sağlar. Bu tez yazısında iki spektrometre teknolojisinin avantajları doğrultusunda birleştirilerek oluşturulan hibrit bir spektrometre tasarımı anlatılmaktadır. Tasarımın dağıtıcı kısmı tüm muhtemel optik sapınç ve sinyal alçalması kaynakları hesaba katılarak simüle edilmiştir. Bununla birlikte, tasarımın interferometre kısmı ise hareket eden aynaların dinamiği üzerine özen gösterilerek kurulmuş ve test edilmiştir. Tasarımımıza en uygun yapıyı bulmak amacı ile çeşitli yöntemler keşfedilmiştir.

Thesis Supervisor: Meriç Özcan

Title: Associate Professor, Department of Electronics Engineering,
Sabanci University

Acknowledgments

I would like to express my thankfulness to my supervisor Assoc. Prof. Dr. Meriç Özcan for his helpful comments, inspiring ideas and useful notices during the learning process at Sabanci University. As an aspiring Master's student, I learned much from his deep knowledge and approach.

I would also like to thank to the committee members of my thesis defense Prof. Dr. Erkey Savas and Prof. Dr. Necati F. Ecevit for their interest and useful criticisms. Moreover, I also would like to thank to my dear colleague Behzad Sardari for contributing and helping me out while dealing with diverse difficulties.

Likewise, I appreciate the support of The Scientific and Technological Research Council of Turkey (TÜBİTAK) for this project named “Development of Fast and High Resolution Raman Spectrometer” under the research fund No: 113F357.

Finally, I would like to thank my family and my friends for supporting and encouraging me during my whole training process in my Master's studies.

Contents

1	Introduction	13
1.1	Scope of this thesis	13
1.2	Theory of the Michelson interferometer	14
1.3	Raman spectroscopy, a brief introduction	18
2	Overview of IR spectroscopy	21
2.1	FTIR spectroscopy	21
2.2	Dispersive Raman spectrometers	22
3	Proposed setup: a hybrid FTIR and dispersive spectrometer	25
4	Optical design	28
4.1	Design tools	28
4.2	Dispersive optics	29
4.2.1	The optical elements displacement: input slit, grating and mirrors	29
4.2.2	Aberrations in dispersive Raman	33
4.2.3	Optimization of the CCD location and line spread function	37
4.3	Interferometer design	41
4.3.1	Framework for interferometer design and simulation . .	41
4.3.2	Collecting optics and fiber coupling	47
5	Design of the chassis	49

6	Experimental results and data processing algorithms	52
6.1	Rotating mirror setup	53
6.1.1	Rotating mirrors assembly	53
6.1.2	Sliding mode control	56
6.2	Piezomotor implementation	60
6.3	Linear motor experiments	69
7	Conclusions and future works	77

List of Figures

1-1	Michelson interferometer schematic.	17
1-2	Light path length increases $2\Delta d$ for a mirror displacement of Δd	18
1-3	Spectrum of the acetone molecule.	20
2-1	Michelson interferometer as used in our setup: the collimated beam that enters the beamsplitter, is split in two beams that are reflected by the fixed and translating mirrors. The recombined beam is then focused on a slit and enters the dispersive part afterward.	22
2-2	Diffraction grating splitting the incident beam into multiple modes.	23
3-1	The proposed setup is composed by three parts: the input Raman probe shines a laser signal onto a sample and collects the scattered light, coupling it to a multimode fiber. The light enters through a collimating lens system the FTIR spectrometer; the beam, after it is recombined in the beamsplitter, is then focused by a curved mirror on a pinhole, and then enters the dispersive section. Finally a CCD camera collects the diffracted light.	27
4-1	The software orchestration architecture, as explained in the text.	29
4-2	The plot of the intensity of interfered light as function of k	30

4-3	Beam entering the dispersive setup is collimated by the collimating mirror onto the diffraction grating.	31
4-4	Complete simulation of the Czerny-Turner configuration. 10 wavelengths equally spaced from 430 to 1300 [nm] are sent through the system using ray tracing simulation.	32
4-5	Angle between the diffraction grating and the first negative order.	33
4-6	Angles between the optical elements (a) and their dimensions in [mm] (b).	34
4-7	The effect of the astigmatism is displayed. Rays focus at different points in the sagittal and tangential planes.	36
4-8	Effect of the spherical aberration on the focused rays.	38
4-9	Focal distance distribution for wavelengths hitting the focusing mirror on different locations (dashed), and fitting line (solid).	38
4-10	Pointcarré map of an off location of the CCD (a) and of the optimal location of the CCD (b). The guard bars are to indicate the height of the CCD.	40
4-11	LSF (corresponding to the maps in Figure 4-10) of an off location of the CCD (a) and of the optimal location of the CCD (b).	40
4-12	The zero padded input plane electric field for a specific wavelength (a) and the interference image (b) are displayed.	44
4-13	The plot of the average intensities of the pixels matrix (a) and the plot of its Fourier transform where the three peaks (in $[m^{-1}]$) of the interfered wavelengths are well detectable.	44
4-14	The interferometer depicted has the mirror on the top slightly tilted, producing an incomplete interference on the detector.	45
4-15	Interference pattern: on the top the fully destructive interference for an aligned mirror and a tilted mirror, on the bottom the constructive interferences.	45

4-16	Drop in the dynamic range as function of the tilt angle of the mirror.	46
4-17	Role of the maximum acceptance angle α on the design of the Michelson interferometer, as explained in the text.	48
5-1	(a) Overview of the chassis and the components location. (b) Top view of the chassis. 1-the chassis; 2-the 2 DOF beamsplitter holder; 3-the translating stage; 4-the diffraction grating turret; 5-the pinhole holder; 6-the fiber input mount; 7-the collimating lens; 8-the fixed mirror	51
5-2	Design of the translating mirror holder, housing 0.5 [in] mirrors, to be placed on the top of the motion stage.	51
6-1	(a) The light travels through the mirrors assembly that creates a delay of 13 [mm] in this configuration. A shorter mirror is mounted to allow a longer scanning range. (b) The assembled setup is created from machined ABS plastic: the manufactured rotating stage is composed by the spinning mirrors mounted on a BLDC motor, the fixed mirror on the right and the inlet hole on the left.	55
6-2	Delays obtained for two simulations. X axis is the discrete time intervals where ray propagation is performed, Y axis is the absolute delay in mm. In the first plot a shorter mirror is employed, while in the second plot two mirrors of the same length are mounted.	56
6-3	Raman spectrum obtained from acetone sample, and the background noise in the second plot.	56
6-4	Clarke, on the left, and Park, on the right transforms.	57

6-5	Schematics of the sliding mode control as explained in the text. The red blocks are the inner current loops, closed directly on the current feedback of the motor. The outer black loop is the speed control, closed through the sliding mode observer, instead of the encoder data that would be seen on traditional PID controls. .	58
6-6	The sliding mode observer takes as input the voltages and currents from the Park transform, and simulates the operation of a drive. The first part is the electrical dynamics, where the resistance R and the inductance L of the coils are considered. The second part, linked to the first one by the machine constant K_s , emulates the mechanical dynamics, taking into consideration the friction F and the inertia J. Angle and speed signals are the output, and low pass filtered to ensure smoothness for the next steps.	59
6-7	First plot is the reference speed (blue) and angle (green) from the plant, and second one from the sliding mode observer. Speeds and angle slopes are in good agreement.	60
6-8	The PI motion stage used in this setup.	61
6-9	The interferometer setup as described in the text.	62
6-10	Schematics of the data acquisition process: the start button issues a global trigger to the motion stage and to the camera; it is also collected by the acquisition board. The acquisition board records the triggers from the camera and from the motion stage.	63
6-11	This is the timings chart of the signals recorded on the acquisition board: the first signal is the camera trigger, occurring at a constant rate; the second signal is the motion stage trigger, they are uniform in space ($5 [\mu\text{m}]$ apart), but not uniform in time. The third signal is the start trigger, and the last signal is a convenience switch to start the data acquisition in Matlab. .	63

6-12	Bouncing effect on the micropositioner signal, the spurious edges are marked with a red cross.	65
6-13	The interpolated data: points marked with a + are the actual rising edges of the stage triggers, while the points marked with * are the interpolated data.	66
6-14	Simplified schematic of a linear stage driven by a piezo motor: the PZT elements (gray) are fired alternatively at a constant frequency to translate the stage.	66
6-15	Three red LED light spectrums acquired with the piezo motor setup. (a) is acquired with a driving frequency of the stage of 10 KHz, (b) at 20 KHz and (c) at 25 KHz. The side bands are possibly due to the vibration of the stage that is acting as a modulation on the acquired signal.	68
6-16	Spectrum of a 785 [nm] laser acquired with a driving frequency of the stage of 25 KHz. The effect of the vibration of the stage is noticeable in the quite broad spectrum of the peak (about 15 [nm]).	68
6-17	Interferometer schematics: the blue light path is the main beam, it is expanded by a microscope objective, collimated, and sent through the interferometer, falling afterward on the CCD camera. The red path is the reference beam, it follows the opposite path of the main beam.	70
6-18	Picture of the interferometer with the main (blue) and reference (red) beams.	71
6-19	A few cycles of the reference beam interference, with the zero crossing points marked with orange circles.	72
6-20	Image of the fiber mode acquired by the camera, used to perfectly align the two interferometer arms.	73

6-21	White light spectrum interference recorded with the camera. The interference occurs at the point where the interferometer arms have the same length.	73
6-22	Time signal and its corrected Fourier transform for an infrared LED.	75
6-23	Time signal and its corrected Fourier transform for a yellow LED with a 785 [nm] laser light superimposed.	76

List of Tables

4.1	The parameters used to calculate the position of an astigmatism correcting cylindrical lens.	36
-----	---	----

Chapter 1

Introduction

1.1 Scope of this thesis

Spectroscopy is a widely used technique to identify chemical compounds, and finds applications in many fields; it is used from food analysis to forensics. This thesis is part of a project that aims to develop a novel FT spectrometer that overcomes most of the limitations of actual spectrometers of this type. In FT spectrometers the beam that needs to be analyzed enters a Michelson interferometer and interferes on a single detector, here we want to multiplex this signal by splitting it into multiple channels, each of a fixed bandwidth, and use a CCD linear detector to acquire the signal. This technique enables us to improve the sensitivity of the instrument because the fluorescence, all FT spectrometers are susceptible of, will be distributed and this would increase the SNR of all detectors. Current FT spectrometers are bounded to the infrared region as fluorescence is reduced, but this new configuration will enable the spectrometer to detect clean signals in the visible and UV region as well. This is not only an improvement in the instrument bandwidth, but also allows excitation of the sample at lower wavelengths, producing a higher intensity signal, as in the case of Raman spectroscopy.

In this thesis the system composed by the Michelson interferometer and the dispersive section that splits the interfered beam into multiple channels is

designed, and the Michelson interferometer is built and tested with different solutions for the implementation of the delay line. The natural followup of this thesis will be the implementation of the complete system, following the optical design proposed here.

1.2 Theory of the Michelson interferometer

The Michelson interferometer is the best known of a class of interferometers known as amplitude splitting interferometers; when used to detect the spectrum of light, a fixed mirror is replaced by a translating mirror, to introduce a delay in one of the interferometers arm, making it an interferometric auto-correlator.

In a Michelson interferometer as depicted in Figure 1-1, the electric field $E = E_0 \sin(\omega t + \phi)$ is split into two equal beams, E_1 and E_2 :

$$E_1 = E_0 \sin(\omega t + \phi + L_1 k) \quad (1.1)$$

$$E_2 = E_0 \sin(\omega t + \phi + L_2 k) \quad (1.2)$$

$$(1.3)$$

where ω is the frequency, ϕ the phase and $k = 2\pi/\lambda$ is the wavenumber, then the electric field E_i falling on the detector is the superposition of the two fields $E_i = E_1 + E_2$.

Assuming a constant $E_0^2 = I_0$, the intensity I is:

$$\begin{aligned}
I(\tau, k) &= |E_i|^2 = |E_1 + E_2|^2 \\
&= I_0 \sin^2(\omega t + kL_1 + \phi) + I_0 \sin^2(\omega t + kL_2 + \phi) + \\
&\quad + 2I_0 \sin(\omega t + kL_1 + \phi) \sin(\omega t + kL_2 + \phi) \\
&= I_0 \left(\frac{1 - \cos(2\omega t + kL_1 + \phi)}{2} \right) + I_0 \left(\frac{1 - \cos(2\omega t + kL_2 + \phi)}{2} \right) + \quad (1.4) \\
&\quad + I_0 [\cos(k(L_1 - L_2) - \cos(2\omega t + 2\phi + k(L_1 - L_2)))] \\
&= I_0 [(1 + \cos(k(L_1 - L_2)))] \\
&= I_0 [(1 + \cos(k\tau))]
\end{aligned}$$

where τ is $L_1 - L_2$, the difference between the arms length of the interferometer. The cosine terms having the time t in the argument have time average equal to 0.

This was derived for a single wavelength (monochromatic signal); in general we would have a distribution of wavelengths (wavenumbers), then $I(\tau, k) = I(k)[(1 + \cos(k\tau))]$. The total intensity measured by the photodetector at every path length difference τ is:

$$\begin{aligned}
I(\tau) &= \int_0^{+\infty} I(\tau, k) dk \\
&= \int_0^{+\infty} I(k)[(1 + \cos(k\tau))] dk \\
&= \int_0^{+\infty} I(k) dk + \int_0^{+\infty} I(k) \cos(k\tau) dk \quad (1.5) \\
&= \frac{1}{2} \int_{-\infty}^{+\infty} I(k) dk + \frac{1}{2} \int_{-\infty}^{+\infty} I(k) \cos(k\tau) dk \\
&= \frac{1}{2} I(\tau = 0) + \frac{1}{2} \int_{-\infty}^{+\infty} I(k, \tau) \cos(k\tau) dk
\end{aligned}$$

that is the cosine Fourier transform of $I(k)$, composed by a DC term, $I(\tau = 0)$

and a modulated AC term. From here we can write:

$$\int_{-\infty}^{+\infty} I(k) \cos(k\tau) d\tau = 2[I(\tau) - \frac{1}{2}I(\tau = 0)] \quad (1.6)$$

Finally, from the recorded intensity signal as a function of the delay τ , we can obtain the spectral density $I(k)$ by taking its inverse cosine Fourier transform:

$$\begin{aligned} I(k) &= \int_{-\infty}^{+\infty} 2[I(\tau) - \frac{1}{2}I(\tau = 0)] \cos(k\tau) d\tau \\ &= 2 \int_0^{+\infty} 2[I(\tau) - \frac{1}{2}I(\tau = 0)] \cos(k\tau) d\tau \\ &= 4 \int_0^{+\infty} [I(\tau) - \frac{1}{2}I(\tau = 0)] \cos(k\tau) d\tau \end{aligned} \quad (1.7)$$

Since the values of $I(\tau)$ are all real, this is equivalent to the inverse Fourier transform of $I(\tau)$:

$$I(k) = FT^{-1}[I(\tau)] = 4 \int_0^{+\infty} [I(\tau) - \frac{1}{2}I(\tau = 0)] e^{ik\tau} d\tau. \quad (1.8)$$

For practical reasons the scanning length is reduced in a range $[-L/2, L/2]$, that is equivalent to multiply $I(\tau)$ with a boxcar function of size $[-L/2, L/2]$. We can rewrite the FT integral as:

$$I(k) = 2 \int_{-L/2}^{+L/2} [I(\tau) - \frac{1}{2}I(\tau = 0)] e^{ik\tau} d\tau = 2 \int_{-\infty}^{+\infty} \Pi(\frac{\tau}{2L}) [I(\tau) - \frac{1}{2}I(\tau = 0)] e^{ik\tau} d\tau. \quad (1.9)$$

The FT of the boxcar function is the sinc function, hence this operation is equivalent to convolve the input signal with the instrument resolution function $\text{sinc}(2Lk)$ that has the first zero at

$$\Delta(k) = \frac{1}{2L}. \quad (1.10)$$

It is clear that to increase the resolution of the instrument it is simply necessary to increase the traveled distance L .

Let us now consider a discretized input signal composed by N equally spaced intensities samples, with index n running from 0 to $N-1$; each sample is spaced $L/N = \Delta d$, where L is the total path length difference, and $\tau_n = n\Delta d$. The discrete Fourier Transform will be:

$$I(k_n) = \sum_{n=0}^{N-1} I(\tau_n) e^{ik_n\tau_n}. \quad (1.11)$$

where k_n is the discretized wavenumber. The Nyquist criterion sets the maximum step distance Δd to avoid aliasing: if $k_s = \frac{2\pi}{\Delta d}$ is the sampling frequency in wavenumber, $k_n = \frac{\pi}{2\Delta d}$ is the maximum detectable wavenumber, or Nyquist wavenumber.

For instance, if we have a spectral range from 400 [nm] to 1100 [nm] (or 157080 to 57120 [cm^{-1}]), the sampling steps Δd must be at most a quarter of the shortest wavelength, namely 100 [nm] (or 628320 [cm^{-1}]); in fact the path traveled by the light beam increases by $2\Delta d$ for each step Δd of the mirror, as shown in Figure 1-2.

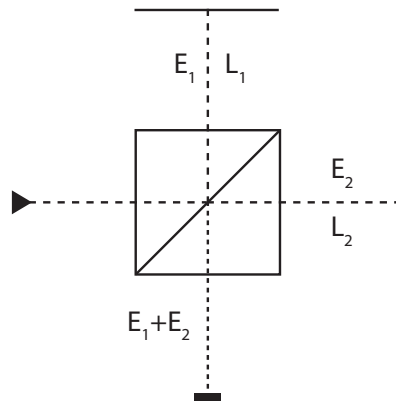


Figure 1-1: Michelson interferometer schematic.

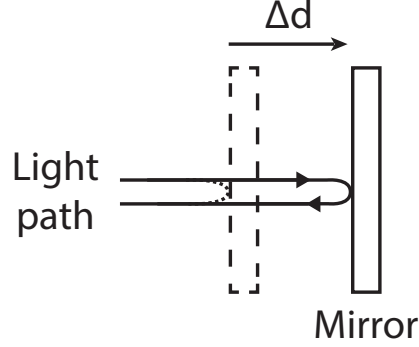


Figure 1-2: Light path length increases $2\Delta d$ for a mirror displacement of Δd .

1.3 Raman spectroscopy, a brief introduction

Raman spectroscopy is one of the spectroscopy techniques first discovered by Chandrasekhara Venkata Raman, an Indian physicist, in 1930. This technique exploits the characteristics of any molecule, of having specific vibration modes, that are discretely quantized [1]:

$$P = \alpha \bar{E}, \quad (1.12)$$

where P is the strength of the induced dipole mode, α is an instantaneous function of the current position of the atoms in the molecule, and (\bar{E}) is the intensity of the incident wave, represented as

$$E = E_0 \cos(2\pi\nu_0 t). \quad (1.13)$$

If we select Q as the physical displacement about their equilibrium position, a vibration mode can be expressed as:

$$dQ = Q_0 \cos(2\pi\nu_{vib} t), \quad (1.14)$$

where Q_0 is the maximum displacement about the equilibrium position. The polarizability can be approximated to the first order Taylor expansion as:

$$\alpha = \alpha_0 + \frac{d\alpha}{dQ} dQ = \alpha_0 + \frac{d\alpha}{dQ} Q_0 \cos(2\pi\nu_{vib} t), \quad (1.15)$$

where α_0 is the polarization of the molecule at the equilibrium point.

Finally we can write:

$$P = \alpha_0 E_0 \cos(2\pi\nu_0 t) + \frac{d\alpha}{dQ} Q_0 E_0 \cos(2\pi\nu_{vib} t) \cos(2\pi\nu_0 t). \quad (1.16)$$

Expansion of $\cos(2\pi\nu_{vib} t) \cos(2\pi\nu_0 t)$ yields to a significant result:

$$\frac{1}{2} \cos(2\pi(\nu_0 - \nu_{vib})t) \cos(2\pi(\nu_0 + \nu_{vib})t), \quad (1.17)$$

In the above equation it is clear how the molecule will vibrate, other than at the frequency ν_0 , the elastic vibration, at two other modes: $\nu_0 \pm \nu_{vib}$, the inelastic vibrations.

The so called Rayleigh scattering corresponds to the light emitted at the incident frequency ν_0 , while the up and down shifted scattering are the Raman scattering, more precisely the stokes $\nu_0 - \nu_{vib}$ and anti-stokes $\nu_0 + \nu_{vib}$. The only condition for the existence of the Raman scattering is the fact that $\frac{d\alpha}{dQ} \neq 0$ [2]. This means that a vibrational displacement of the atoms in the molecule must reflect on a change in the polarizability α . Stokes scattering is the one that carries more power, hence the easiest to detect. A simplified explanation is that, according to the Boltzmann equations, more molecules should be in the ground state than in any excited one. The exciting wavelength selection plays a crucial role in the design of a Raman spectrometer, since Raman signal intensity is roughly proportional to the inverse of the fourth power of the incident wavelength, meaning that shorter wavelengths result in a more powerful signal. On the other side as the wavelength gets shorter, another inelastic phenomena, called fluorescence, can obscure the Raman signal. It is also to be noted that a larger wavelength leads to a larger shift, making the Raman signal easier to isolate. An optimal compromise has to be found.

There are mainly two different setup, the FTIR spectrometer and the dispersive spectrometer. The first one usually employs a Michelson interferometer in which a mirror is fixed and the other is translating, scanning a distance that

is linked to the resolution of the instrument by the formula

$$res[cm^{-1}] = \frac{1}{delay_{MAX}[cm]}, \quad (1.18)$$

where res is the resolution and $delay_{MAX}$ is the maximum achievable optical delay. This is because, as the Fourier transform of a signal in time domain belongs to the reciprocal of that domain (frequency), the FT of a signal in the length domain appertain to the wavenumber domain. The second type of setup is the dispersive spectrometer, that uses a diffraction grating to split the wavelengths and fan them out on a CCD. In the typical configuration, the beam enters from a slit, and expands with a known NA on a collimating mirror. It is then steered onto a diffraction grating that splits the beam, and one of the diffraction modes is collected by a focusing mirror and focused on a linear CCD array. An example of a Raman chart, obtained in our lab with a dispersive spectrometer is shown in Figure 1-3.

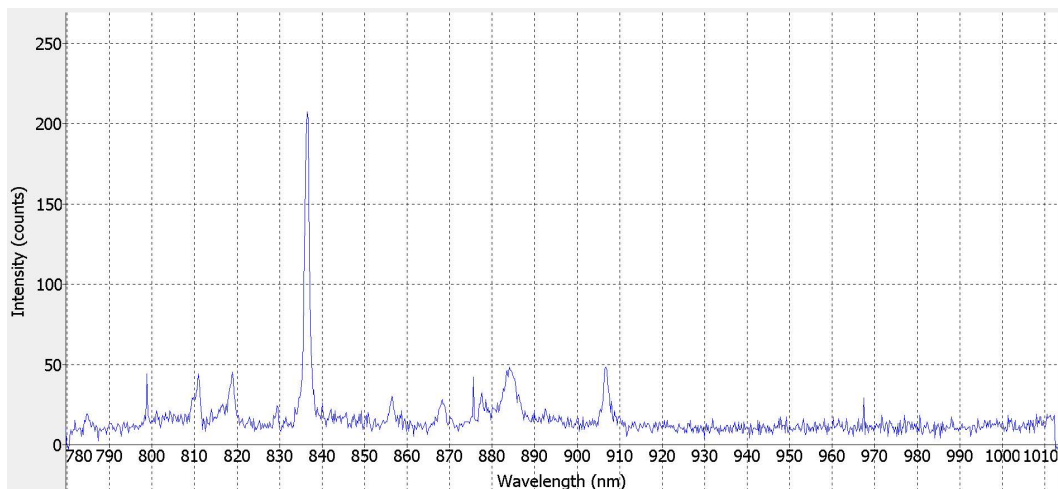


Figure 1-3: Spectrum of the acetone molecule.

Chapter 2

Overview of IR spectroscopy

2.1 FTIR spectroscopy

FT-Raman Spectrometers are much faster and they have the capability for higher resolution when compared to the dispersive type [3], but they are more vulnerable to fluorescent noise since all spectral components are recorded simultaneously. The excitation source's wavelength should be much longer to avoid the interference of noise originating from the fluorescent light. The most common excitation source for these spectrometers is Nd-Yag at 1064 nm in order to have reduced background noise [4]. Due to this excitation wavelength, causing it to have reduced sensitivity level, FT-Raman is generally confined to routine bulk analysis in recent times. FT-Raman spectrometer is based on the most common of all interferometers, namely the Michelson interferometer. A typical Michelson interferometer consists of one stationary mirror, one translating mirror and a beam splitter at the center as shown in Figure 2-1. The beam splitter is usually a 50:50, meaning that half of the incident power is transmitted and half is reflected. While one of the waves is reflected off the stationary mirror traveling a distance of $(2L)$, the other wave is reflected off the moving mirror traveling a distance of $(2L+2d)$ where 'd' is the traveled distance of the translating mirror from the central position. The returning waves interfere with each other forming an interference pattern on the detector, be-

cause it is a well known fact that if the optical path difference ($2d$) is equal to a multiple of the wavelength, a constructive interference occurs, and the vice-versa occurs if ($2d$) is equal to $(n + 0.5)\lambda$. Naturally, the resulting values are detected in the space domain, and the Fourier Transform of this function yields the spectrum of the incoming signal, in the wavenumber domain.

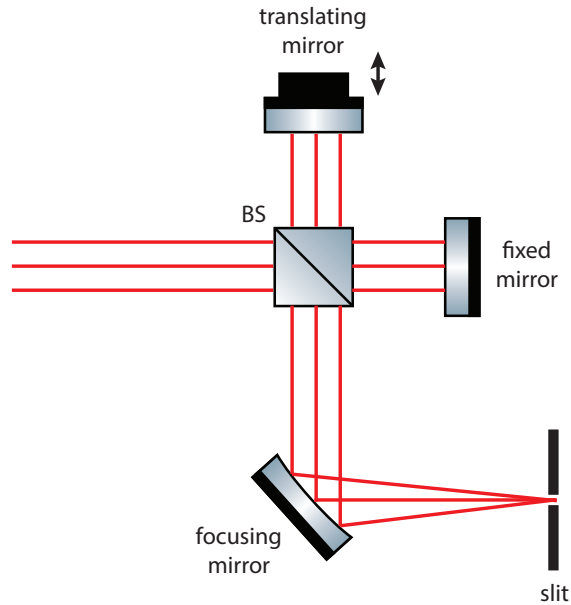


Figure 2-1: Michelson interferometer as used in our setup: the collimated beam that enters the beamsplitter, is split in two beams that are reflected by the fixed and translating mirrors. The recombined beam is then focused on a slit and enters the dispersive part afterward.

2.2 Dispersive Raman spectrometers

Dispersive Raman spectrometers are nowadays much more common than FTIR ones, because of their compactness, robustness, and price. The working principle of a Dispersive spectrometer is as follows: the Raman scattered light, emitted from a compound in the sample room as a result of an interaction between that compound and the incident wave, is collected with a lens and passed through a slit. It is then steered by a collimating mirror towards a

diffraction grating, which is the key element in the system. Subsequently, the grating splits the spectrum of the incoming signal into bands of frequencies obeying the following grating equation [5]

$$d(\sin(\theta_i) + \sin(\theta_m)) = m\lambda \quad (2.1)$$

where θ_i is the angle of the incident wave, θ_m is the angle between the diffracted ray and the grating's normal vector, d is the distance between two adjacent slits or grooves and m is the diffraction order. A schematized model is represented in Figure 2-2.

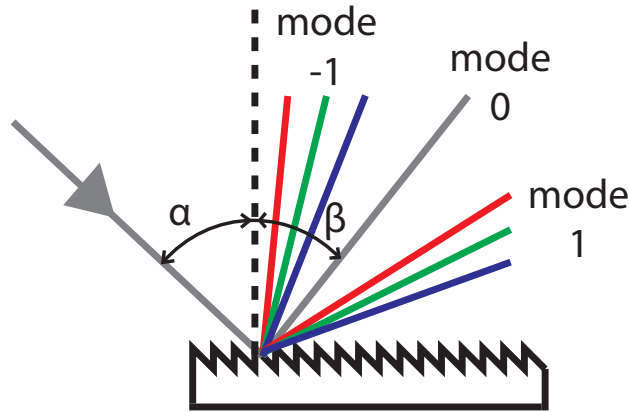


Figure 2-2: Diffraction grating splitting the incident beam into multiple modes.

After the splitting operation is complete, the spectrum is reflected onto a linear detector array to read the intensity information of each frequency band. Now, the designer can choose to use any diffraction order depending on the application, since by simply manipulating the groove period one can determine which diffraction order gets the maximum power. However, the diffracted beams corresponding to consecutive orders may overlap as one goes higher in the spectral order, so it is always wiser to choose to use the first order diffracted beams (either 1 or -1). Dispersive Raman Spectrometers have advantages over FT-Raman Spectrometers in the way that they are less susceptible to

fluorescent noise. Therefore it allows the user to utilize an excitation source with a shorter wavelength. Practically, they can work with excitation sources with wavelengths from UV to NIR range. Considering that the Raman signal intensity is inversely proportional to the excitation wavelength ($\frac{1}{4\lambda}$) [6], this advantage makes Dispersive Raman Spectrometers more preferable in many applications where increased sensitivity is a requirement.

Chapter 3

Proposed setup: a hybrid FTIR and dispersive spectrometer

In this work we propose a -hybrid dispersive and Fourier transform Raman spectrometer- that will perform both in sensitivity and resolution, as opposed to dispersive and FTIR spectrometers that perform in only one of the two aspects. Our aim is to overcome the disadvantages of classical FT-Raman interferometers that are the high fluorescent background noise, especially at low excitation wavelengths, by combining it with a dispersive element so that we can employ an excitation source with smaller wavelengths and therefore more power, significantly increasing the signal to noise ratio at the output. At the same time the advantages of the FTIR spectroscopy, such as the resolution and speed, will still be present. Since with this novel setup we will overcome the fluorescence issue, a lower wavelength of 785 [nm] (common for Raman applications) can be used instead of the 1064 [nm] common for FTIR spectrometers.

This setup is composed by three sections, the Raman probe, the FTIR section and the dispersive section. The schematics of the system is shown in Figure 3-1.

The main purpose of this thesis is to design a hybrid spectrometer composed by a Michelson interferometer on the front and a dispersive spectrometer

after, and the experimentation on the FTIR part. The first part can be considered an FTIR spectrometer, with a fiber coupled Raman probe as input. Two possible scanning mechanisms have been investigated, a rotating setup composed by two mirrors face to face, and a translating mirror. Even though the rotating mirror setup has been discarded in favor of the translating since such a system would require an acquisition speed that can not be achieved by linear or 2D pixel arrays (needed in our setup), an FTIR employing this rotating system has been set up to show its advantages. In fact a rotating stage is much more stable than a translating one, that requires accelerations and decelerations at the end of its run. The final design that employs a translating stage was designed and tested putting emphasis on the difficulties encountered with the use of a piezo motor, and the final choice of a linear motor instead. The dispersive setup has been designed in an iterative process that tries to find the optimal parameters by using FEM analysis. The dispersive part is particularly challenging as many aberrations such as astigmatism and coma can greatly deteriorate the performances of the instrument. Another important issue is the choice of the right CCD, because speed and QE requirements are very high.

A chassis was also designed to accommodate all the optical components, both of the interferometer and dispersive parts. Its structure well fits a specific piezo motor that was chosen during the design process, but that turned out to have some disadvantages with regard to linear motors, and was then discarded.

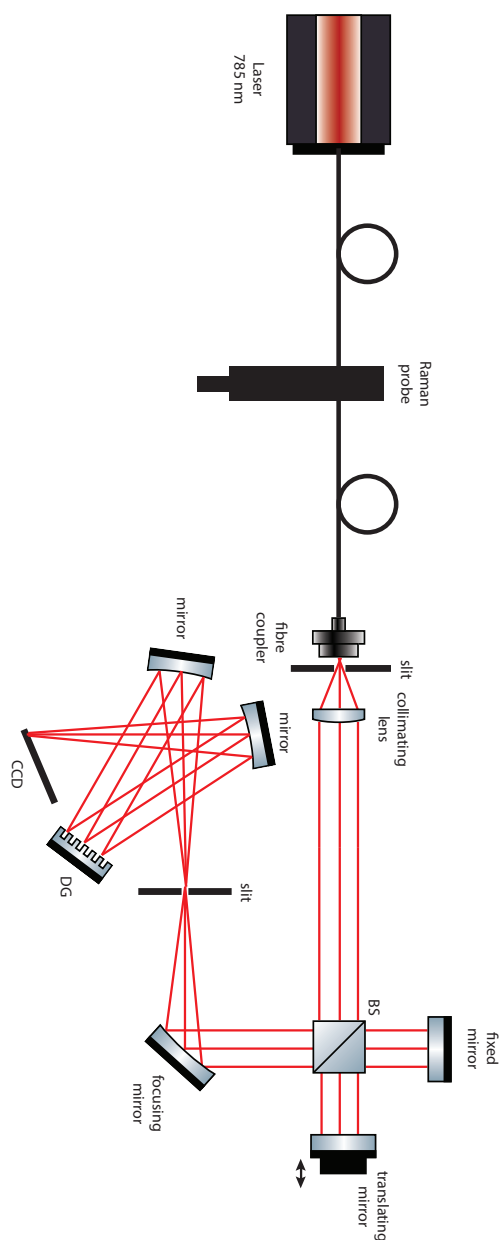


Figure 3-1: The proposed setup is composed by three parts: the input Raman probe shines a laser signal onto a sample and collects the scattered light, coupling it to a multimode fiber. The light enters through a collimating lens system the FTIR spectrometer; the beam, after it is recombined in the beam-splitter, is then focused by a curved mirror on a pinhole, and then enters the dispersive section. Finally a CCD camera collects the diffracted light.

Chapter 4

Optical design

In this chapter I will describe how the dispersive and interferometer parts were designed and merged. The dispersive optics are organized in the common Czerny-Turner configuration, where the slit is placed at the focal point of the collimating mirror, and the other components are placed such that the minimal space is occupied. First I will explain the design of the input optics, namely the slit and the collimating mirror, then the choice of the grating, and the measures to take to minimize the aberrations' effect. Finally the location of the CCD array is optimized to allow a sharp image to be recorded. In the second part the interferometer is designed, underlining the effect of misalignment in the mirrors position; the fiber coupling optics are then designed, as input to the interferometer.

4.1 Design tools

The complex software orchestration developed to design the spectrometer is composed by mainly three components, with very specific functions. The software used to design the mechanical parts is SolidWorks, its special features allowed an easy parametrization of the model parts, and a robust linkage of them as assemblies. Comsol is used as core for the FEM analysis and ray tracing, allowing us to run the simulations on a remote powerful server

machine, and collect the data on a local computer for analysis. The main orchestrator was chosen as MATLAB, that stores the model and properties of our system, and allows us to fully operate on the simulations data. The softwares were linked through the LiveLink interface that Comsol provides. Such a system allows us to run multiple simulations, that imply changes in the geometry, or the properties of the media the rays are travelling into, just by changing the same parameters on the MATLAB script, and automatically reflecting those changes on the SolidWorks design and/or on the Comsol media properties. Finally, after the optimization of the design, the final geometry is loaded on SolidCAM for manufacturing studies and CNC programming. An overview of the complete architecture is given in Figure 4-1.

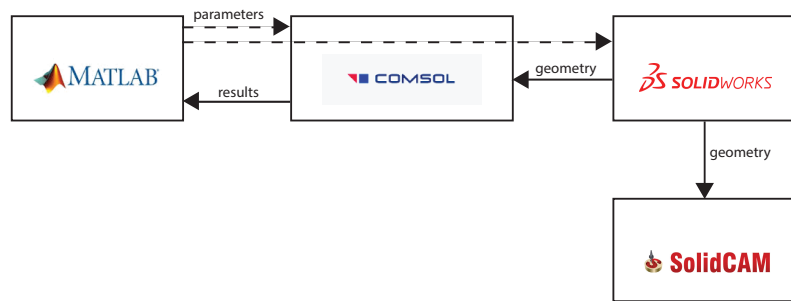


Figure 4-1: The software orchestration architecture, as explained in the text.

4.2 Dispersive optics

4.2.1 The optical elements displacement: input slit, grating and mirrors

Dispersive spectrometers, also called Czerny-Turner spectrometers, are usually designed for F-number greater than 3, to avoid aberrations [7]. F-number is related to NA according to the following equation:

$$F - number = \frac{1}{2NA} \quad (4.1)$$

where NA is the numerical aperture, related to the light cone angle θ by the relation

$$NA = n \sin(\theta) \quad (4.2)$$

where n is the refractive index of the medium.

At the input of the setup is a slit. Plane waves encountering a single aperture of width w are diffracted such that intensity minima occur for angles θ_n relative to the original direction of propagation given by:

$$\frac{NA}{n} = \sin(\theta) = \frac{k\lambda}{w} \quad (4.3)$$

where k is a strictly positive integer, λ is the wavelength and w the width of the slit. The lobe carrying the maximum power is for $k = 1$, as shown in Figure 4-2.

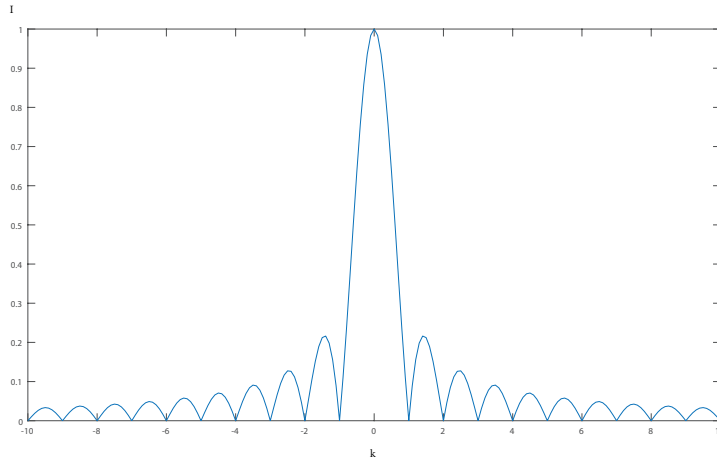


Figure 4-2: The plot of the intensity of interfered light as function of k .

In our case we chose the width of the slit in order to have an F-number of 10. The closest commercially available choice was of 100 [um]. The entrance

slit is at the focal point of the collimating mirror, that is placed at an angle θ_c in order to reflect the beam on the diffraction grating, as shown on Figure 4-3.

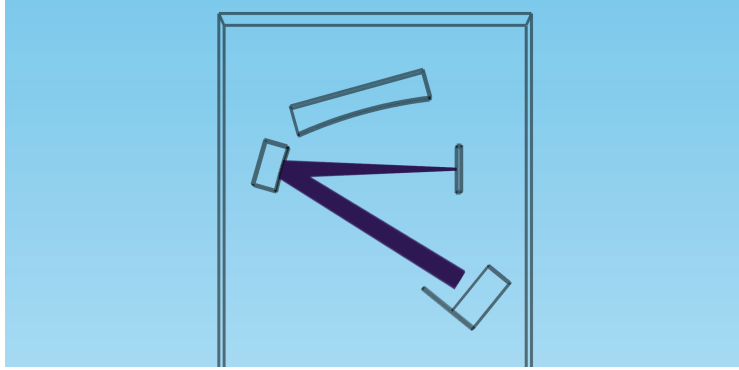


Figure 4-3: Beam entering the dispersive setup is collimated by the collimating mirror onto the diffraction grating.

The grating is placed at the focal point of the focusing mirror, and its angle θ_g angle can be adjusted, to accommodate different grooves density gratings. Finally the focusing mirror is placed at an angle θ_f , that takes one order from the diffraction grating and focuses it on the CCD placed at the focal distance. In our simulation we sent 10 wavelengths equally spaced from 400 [nm] to 1100[nm], from a point source, having a F-number equal to 10. The complete simulation of the system is shown in Figure 4-4

The beam hitting the mirror has diameter of 3.5 [mm] and is collimated on the grating. Diffraction gratings split the incident beam into different wavelengths following the formula [8]

$$d(\sin \alpha + \sin \beta) = m\lambda \quad (4.4)$$

where α is the incident entrance angle and β the reflected angle, d the grooves spacing, m the order and λ the wavelength. Our incident angle, as shown in Figure 4-5, is of 6.7 [deg], m is the order -1 and d was chosen of 300 lines/mm; extrapolating β from the equation above, we can write:

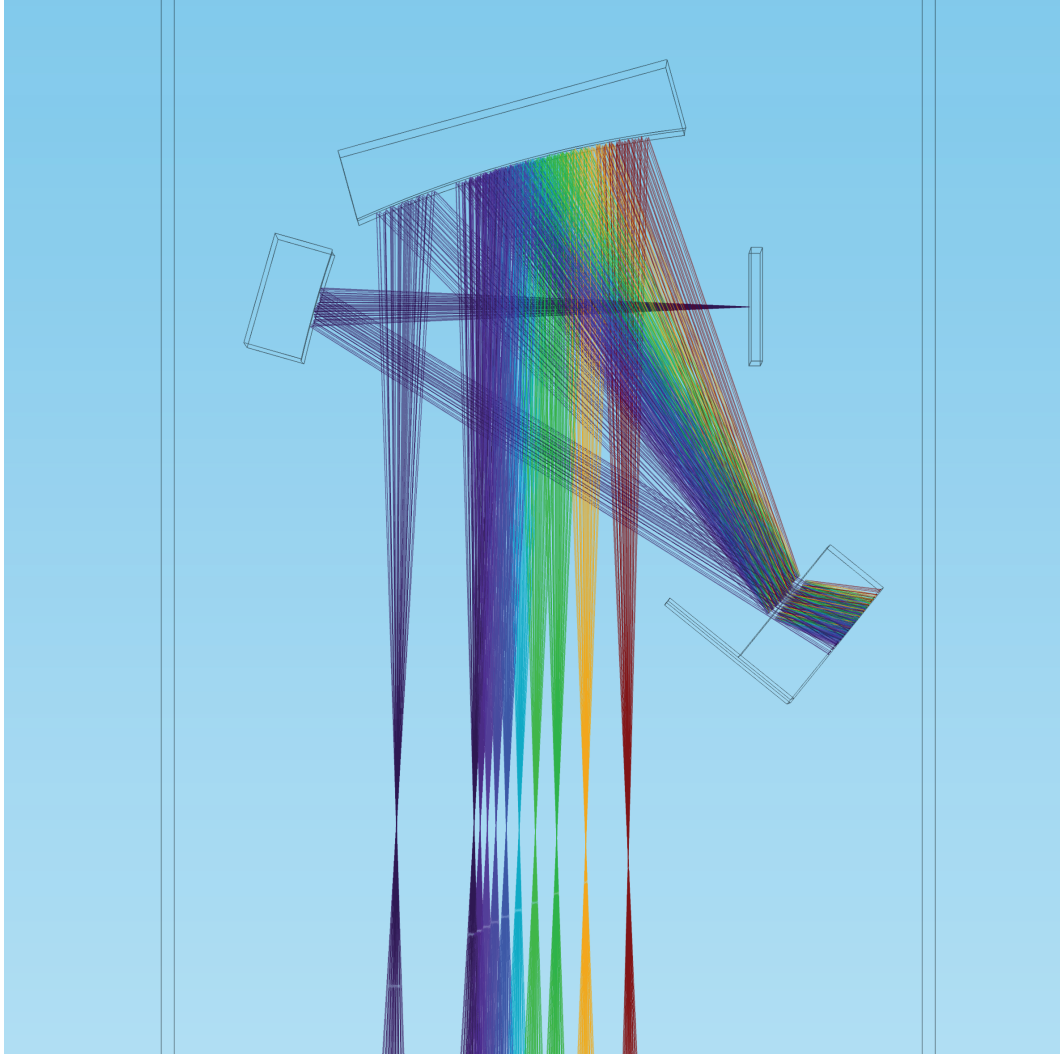


Figure 4-4: Complete simulation of the Czerny-Turner configuration. 10 wavelengths equally spaced from 430 to 1300 [nm] are sent through the system using ray tracing simulation.

$$\beta = \arcsin \frac{m\lambda}{2d} - \sin\alpha = 19.07[\text{deg}] \quad (4.5)$$

for the central wavelength of 700 [nm].

The position and inclination of the diffraction grating has been chosen in order to reflect back to the collimating mirror the order 1 and dispersing it toward the entrance slit. This will avoid this order to cause back reflections that could finally hit the CCD and decrease the SNR. The complete design of the dispersive part, including the angles between the normal vectors of the

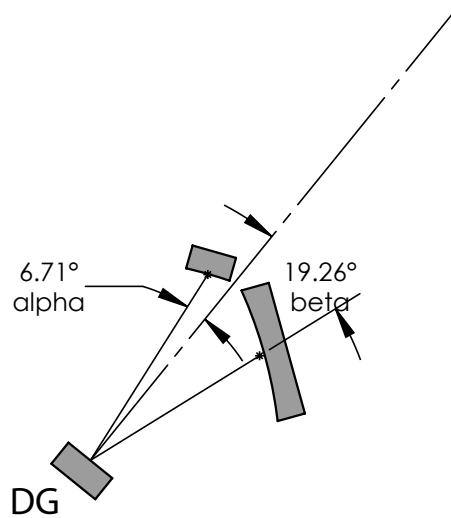


Figure 4-5: Angle between the diffraction grating and the first negative order.

components is shown in Figure 4-6

Although many gratings with different groove density can be fit on the design, the density chosen for the simulation allows about 10 segments, in the spectral range from 400 to 1100 [nm], to be resolved on a 2048 pixels array of 8 [μm] each.

4.2.2 Aberrations in dispersive Raman

Three main aberration phenomenon have to be addressed in the design of a Czerny-Turner based spectrometer, they are coma, astigmatism and spherical aberrations.

Coma Coma is caused by off-axis employment of optical elements such as lenses, mirrors or gratings. Its effect is an asymmetry of the beam (for a specific wavelength), seen as a skewing of rays in the dispersion plane. Coma comes mainly from the asymmetry of the system [9], especially brought by the diffraction grating. This causes the beam leaving the grating to have a different cross-section than the entering beam. This is partially corrected by the focusing mirror, and in our design it is kept to a minimum level by keeping the grating angle the closest to the Blaze angle. Another important rule is to

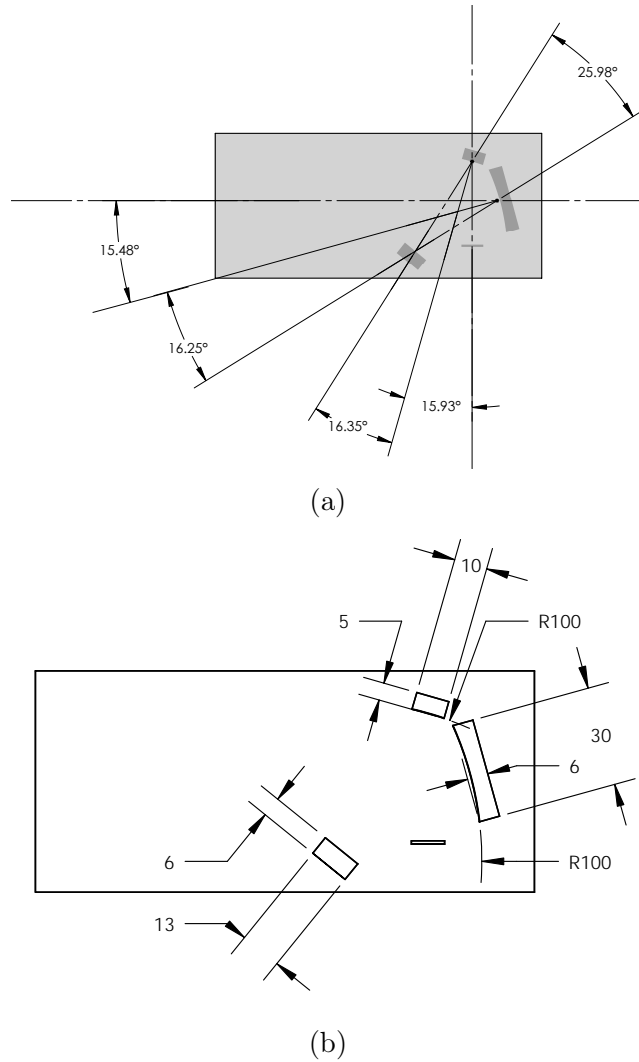


Figure 4-6: Angles between the optical elements (a) and their dimensions in [mm] (b).

keep the radius of the curved mirror the closest possible, in fact our mirrors have both the curvature of 100 [mm].

Astigmatism Astigmatism is the difference in focal length of rays that are parallel and perpendicular to an instrument axis of symmetry. Astigmatism, if limited, has a positive effect because it spreads the beam in the sagittal plane, while keeping it sharp in the tangential plane, as shown in Figure 4-7. Since our CCD pixels columns have a width much shorter than the height, this allows

the beam to be distributed on the whole pixels vertical array; on the other side, an exaggerated astigmatism will cause the beam to extend too much on the vertical plane and fall off the CCD, causing a loss of the signal. Astigmatism comes from the curvature of the spherical mirrors, and the distance between the two foci can be calculated according to the following formula [10]:

$$d_f = \frac{r_1}{2} \sin a_1 \tan a_1 + \frac{r_2}{2} \sin a_2 \tan a_2 \quad (4.6)$$

where r_1 is the radius of the collimating mirror, r_2 the radius of the focusing mirror, a_1 the off-axis incident beam angle on the first mirror, and a_2 on the second mirror. The focal point on the sagittal plane can be calculated as

$$f_s = \frac{r_2}{2 \cos a_2} \quad (4.7)$$

It is possible to correct for astigmatism by fitting a cylindrical lens in the design. The position of such a lens can be calculated as follows:

$$s_{cs} = \frac{P + \sqrt{P^2 + 4P f_{cs}}}{2} \quad (4.8)$$

is the distance of the lens from the new focal point, f_{cs} is the focal length of the cylindrical lens, and P is defined as

$$P = d_f - t_0 \frac{n-1}{n} \quad (4.9)$$

where t_0 is the thickness of the lens. Finally we can define L_c as the distance of the lens from the center of the focusing mirror as

$$L_c = f_s - s_{cs} - t_0 \quad (4.10)$$

we calculated a lens using the parameters in 4.1 and obtained a distance of 37 [mm].

Even though we allocated a place in the design to fit the lens, we choose not to compensate for the astigmatism in the first design, because the beam

r_1	100 [mm]
r_2	100 [mm]
a_1	16 deg
a_2	16 deg
t_0	3
f_{cs}	8
n	1.5

Table 4.1: The parameters used to calculate the position of an astigmatism correcting cylindrical lens.

height at the tangential focal point well fits the pixel column height as it will be shown in the following sections.

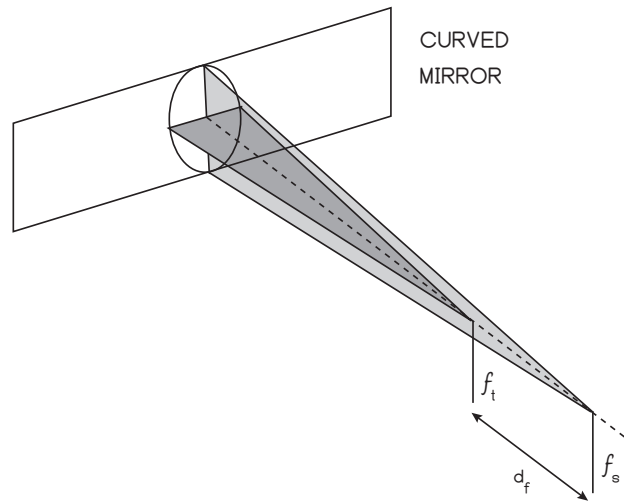


Figure 4-7: The effect of the astigmatism is displayed. Rays focus at different points in the sagittal and tangential planes.

Spherical aberration Finally we must spend some words on the spherical aberration, that comes from the curvature of the focusing mirror. Light hitting different points on the mirror is focused at different distances, as shown in Figure 4-9 for a lens. The focal point of the mirror is dependent on the angle of incidence θ :

$$f = r\left(1 - \frac{1}{2\cos\theta}\right) \quad (4.11)$$

where r is the radius of curvature. For angles $\theta \ll 1$, we can write

$$f = \frac{r}{2} \quad (4.12)$$

In our case we can calculate the effect of the spherical aberration by knowing the range spanned by the diffraction grating, the Blaze angle, and the diffraction angle for different wavelengths:

$$\theta_{450nm} = 16.25 + 1.04 = 17.29[deg] \quad (4.13)$$

$$\theta_{1100nm} = 16.25 - 4.98 = 11.27[deg] \quad (4.14)$$

$$\Delta\theta = \theta_{450nm} - \theta_{1100nm} = 6.02[deg] \quad (4.15)$$

The effect of the incident angle on the radius of curvature is shown in Figure 4-9.

4.2.3 Optimization of the CCD location and line spread function

To adjust the position of the CCD in order to reach an optimal position, the plane of the CCD array was tuned both in distance from the focusing mirror and inclination. Two parameters has been selected, the distance of the CCD plane from the curved mirror, and the inclination with respect to a xz plane.

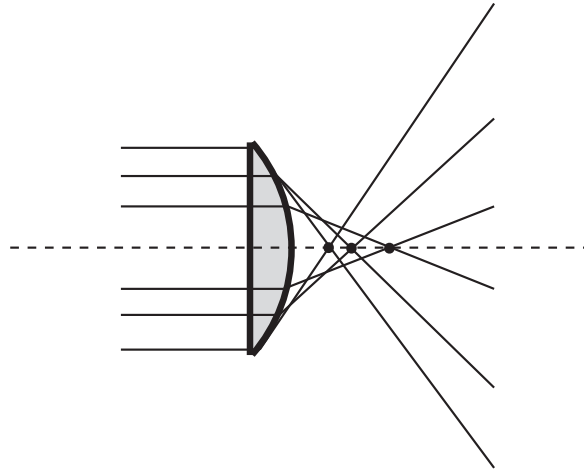


Figure 4-8: Effect of the spherical aberration on the focused rays.

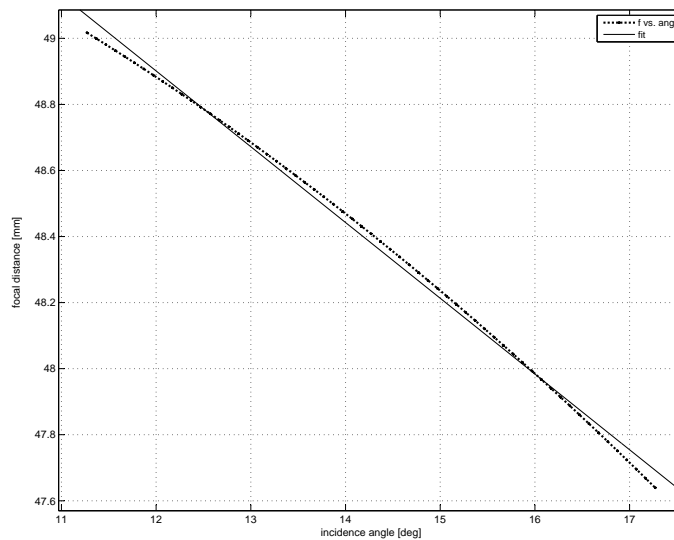


Figure 4-9: Focal distance distribution for wavelengths hitting the focusing mirror on different locations (dashed), and fitting line (solid).

An optimization framework has been set up as follows: using the LiveLink interfaces provided by Comsol (described in Chapter 4.1), the ray propagation was solved in Matlab, and the Pointcarré plot of the rays hitting the CCD plane was analyzed, measuring the maximum distance spanned by each wavelength on the width of the CCD. An optimal function was defined as the rms value of all the distances, and that function was minimized by tuning the distance and

the angle of the plane. Once the optimal parameters were found, they have been used to adjust the position of the CCD in the final design. The focusing of the different wavelengths on a different distance is caused by the spherical aberrations of any spherical optical element: beams closer to the corner of the mirror will focus at a shorter distance. For the selection of the optimal value, a distance of +/- 1 cm has been scanned from the central focal distance of the mirror, and an angle of +/- 15 [deg] has been swept.

The incident beam on the CCD has been analyzed to extract the line spread function (LSF) and estimate the optimal number of sections the beam can be divided into. The cross section of the line image is called a line spread function (LSF). A LSF is derived by integrating the point solid along sections parallel to the direction of the line, in our case the points will be the incident location on the CCD plane of the rays propagated by the ray tracing software. This works because a line image is the summation of an infinite number of image points along its length [11]. Obviously a larger number of rays would increase the “resolution”, giving more accurate results. LSF can be derived from the point spread function (PSF) by integrating it along a line [12]:

$$\text{LSF} = \int_{-\infty}^{+\infty} p(x, -y) dy \quad (4.16)$$

where p is the point spread function, the response of the system to an infinitesimal point source, in our case the single light ray. Since the point spread function can be interpreted as the projection integral of the PSF at different x locations, we can write:

$$\text{LSF} = \int_{-\infty}^{+\infty} p(x, y) dy \quad (4.17)$$

The Pointcarré map (the projection of the rays on a plane perpendicular to their direction) of the CCD plane for a not optimized location, and the optimal location are shown in 4-10; the LSF of the same configurations is shown in Figure 4-11

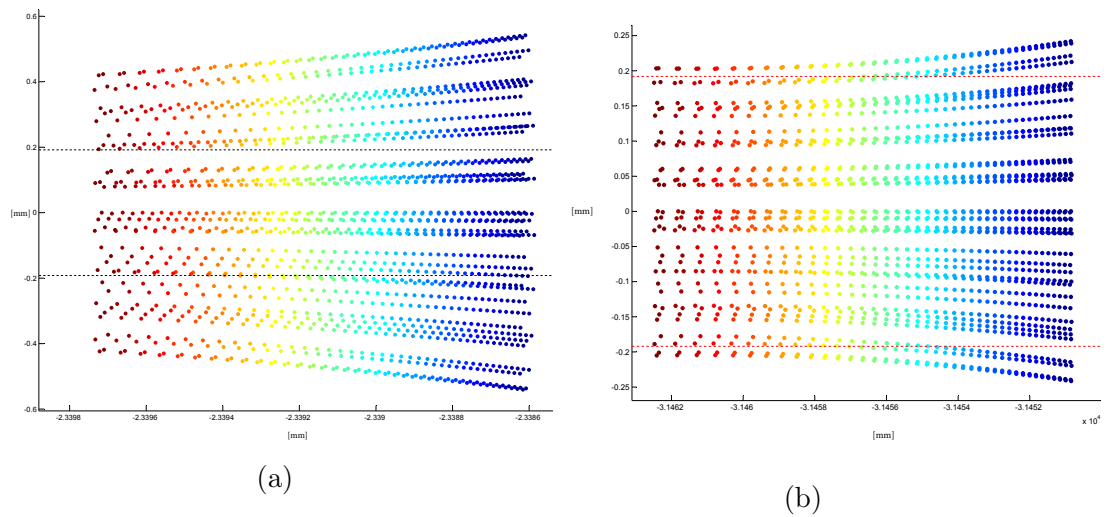


Figure 4-10: Pointcarré map of an off location of the CCD (a) and of the optimal location of the CCD (b). The guard bars are to indicate the height of the CCD.

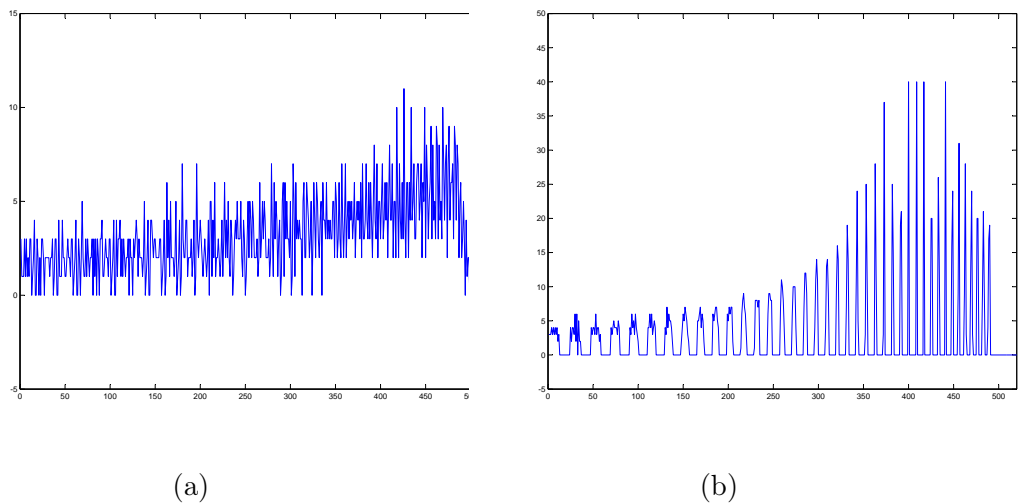


Figure 4-11: LSF (corresponding to the maps in Figure 4-10) of an off location of the CCD (a) and of the optimal location of the CCD (b).

4.3 Interferometer design

4.3.1 Framework for interferometer design and simulation

Design and simulation of the Michelson interferometer was done by using the angular spectrum method to propagate the beam. A MATLAB implementation of the method has been developed. Here follows a brief introduction of the angular spectrum method: this technique models the propagation of a plane wave in a medium, the plane wave is first sampled using a sampling grid on a plane perpendicular to the propagation direction of the field, an FFT of every 'pixel' is taken, and multiplied for a complex function that takes into account the attenuation and the phase change in the medium. To recover and interfere the wave the inverse FFT is taken in the destination plane. Every wavelength is propagated with the same method.

In a more formal approach, the angular spectrum method takes an input source field on the input plane at $z = 0$

$$f(x, y, z) = f(x, y, 0) = \psi_0(x, y) = \int_{-\infty}^{+\infty} \int_{-\infty}^{+\infty} \Psi_0(k_x, k_y) e^{j(k_x x + k_y y)} dk_x dk_y \quad (4.18)$$

where

$$\Psi_0(k_x, k_y) = \mathcal{F}\{\psi_0(x, y)\} \quad (4.19)$$

and a propagation kernel, dependent on the propagation medium [13]

$$h(x, y, z) = \frac{\exp(i2\pi r \lambda^{-1})}{r} z \left(\frac{1}{2\pi r} + \frac{1}{i\lambda} \right) \quad (4.20)$$

where r is the distance of the (x, y, z) point from the center.

The sampling distance of the electric field in the space domain should be fine to avoid aliasing. Also, as the wave propagates, it diffracts and the beam size gets enlarged by the distance it propagates, so the beam size and the zero padding around it should be appropriate for the distance it is supposed to travel. For the first simulation, the beam is supposed to travel for around 30 cm and a beam diameter of 1 mm is both realistic and appropriate for the simulation of an ideal Michelson interferometer. A uniform electric field composed by 3 different wavelengths of 600 [nm], 750 [nm] and 900 [nm] (with the suitable zero-padding) is propagated for the distance mentioned above, the scanning mirror moves by 12.5 [nm] steps (the total path difference is then of 25 [nm]), well below the Nyquist sampling distance that in our case is a quarter of the smallest wavelength (150 [nm]). Higher resolution means higher scanning range, because the resolution in wavenumber is simply the inverse of the scanning range; it is important to note that the wavenumber resolution is not the same for all the wavelengths, in fact a shift in wavelength $\Delta\lambda = \lambda_2 - \lambda_1$ in [nm] corresponds to a Δw in [cm^{-1}] following this equation [14]:

$$\Delta w = \left(\frac{1}{\lambda_1} - \frac{1}{\lambda_2} \right) * 10^7. \quad (4.21)$$

In this simulation 500 samples spaced 12.5 [nm] were taken, yielding to a traveled distance of 6 [μm] hence to a resolution of 1666 [cm^{-1}], enough to separate the sample wavelengths, but allowing a short computational time, being the angular spectrum method a very computational intensive algorithm. The results of the simulation are shown in Figure 4-12 and 4-13.

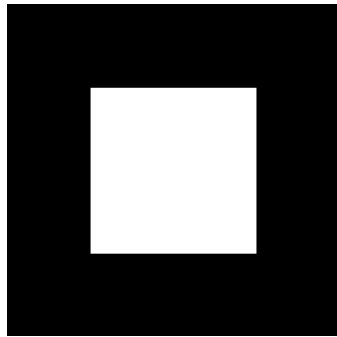
With the method described above, a second experiment was performed, to analyze the effect of misaligned mirrors in the interferometer setup: a beam was propagated for a distance corresponding to the sum of the interferometer arms lengths, d (3 [cm] * 4 = 12 [cm]) and interfered with another beam traveling the same distance plus an incremental scanning distance Δd . In the case of a tilted mirror, the beam travels a longer distance and hit the CCD in a position

that does not fully overlap the interfering beam: it is shifted by a distance that is function of the angle the mirror is tilted, and the arm length:

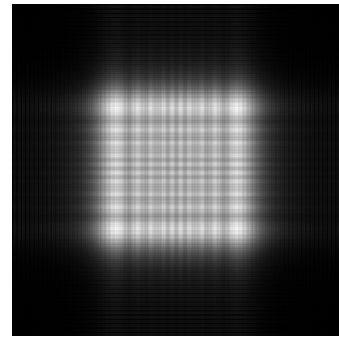
$$S = d \tan \alpha \quad (4.22)$$

where S is the shift amount and α the angle the mirror is tilted with respect to the vector parallel to d . This configuration is shown in Figure 4-14.

The input distribution was sent down the path and interfered with the second beam, and the interferogram recorded. The input plane was taken of the size of 256x256 discrete point sources (pixels) with a size each of 8 [μm], making a 4 [mm²] beam. The interference pattern at each step is recorded, and superimposed for each wavelength, as shown in Figure 4-15. Finally the effect of a tilted mirror was measured as drop in the dynamic range between a fully constructive and a fully destructive interference, and this drop was measured for different angles. The result can be seen in Figure 4-16.

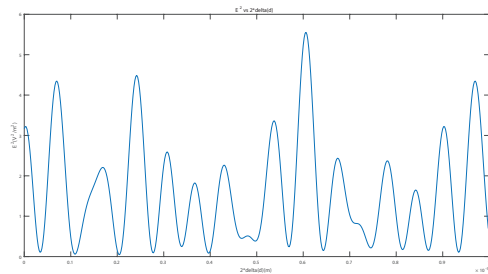


(a)

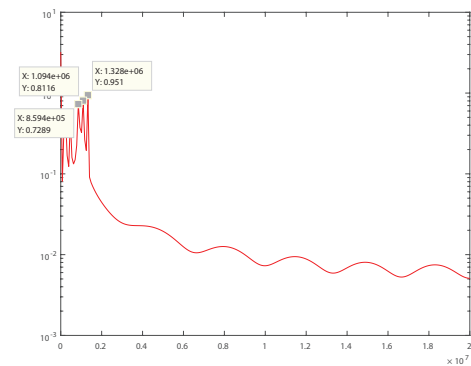


(b)

Figure 4-12: The zero padded input plane electric field for a specific wavelength (a) and the interference image (b) are displayed.



(a)



(b)

Figure 4-13: The plot of the average intensities of the pixels matrix (a) and the plot of its Fourier transform where the three peaks (in $[m^{-1}]$) of the interfered wavelengths are well detectable.

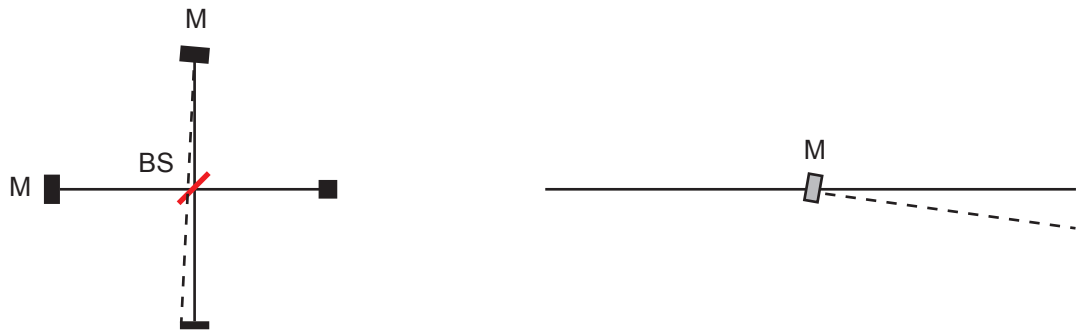


Figure 4-14: The interferometer depicted has the mirror on the top slightly tilted, producing an incomplete interference on the detector.

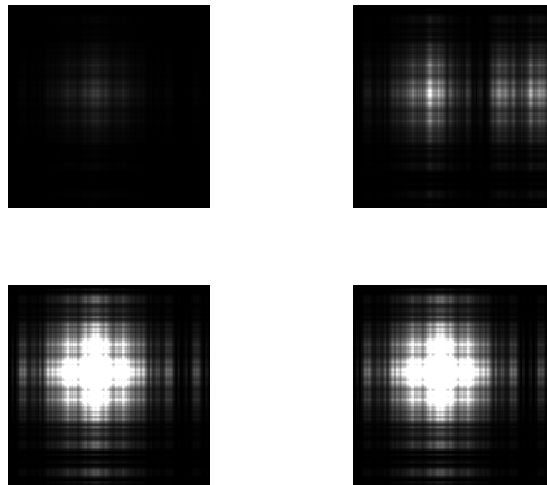


Figure 4-15: Interference pattern: on the top the fully destructive interference for an aligned mirror and a tilted mirror, on the bottom the constructive interferences.

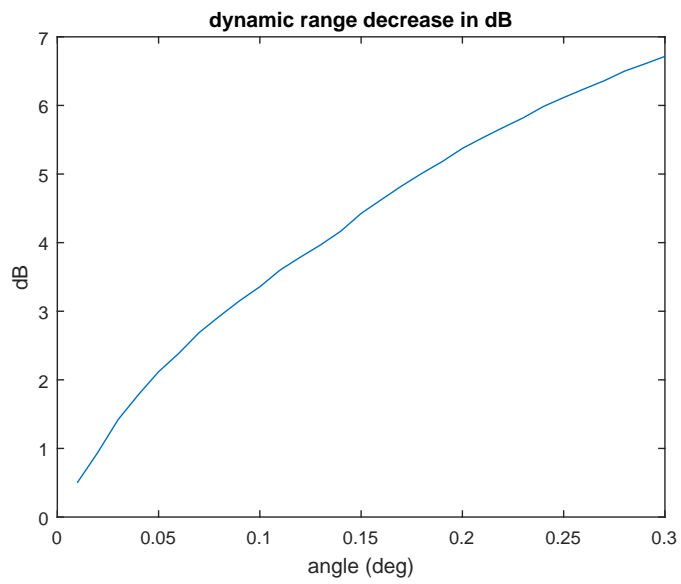


Figure 4-16: Drop in the dynamic range as function of the tilt angle of the mirror.

4.3.2 Collecting optics and fiber coupling

The Raman signal is collected by a commercial probe [15] that carries the 785 [nm] laser to the tip and illuminates a sample. This probe is designed to operate above the 785 [nm], and can be replaced with a probe operating in a different range, if needed. The signal is then filtered inside the probe by a notch filter and sent through a multimode fiber. The input fiber to our setup is a hard polymer-clad, multimode, step-index fiber with a core diameter of 200 μm . Its NA is 0.22. Considering the NA of the fiber, if we do not employ any pinhole to maximize the amount of light entering the system, the light cone angle will be

$$\beta = \arcsin(NA) = \arcsin(0.22) = 0.2218[\text{rad}] = 12.71[\text{deg}] \quad (4.23)$$

Another important parameter is the maximum acceptance angle of the system. It is calculated according to the resolution formula [16]:

$$\alpha_{max} = \sqrt{\frac{\Delta\sigma}{\sigma_{max}}} \quad (4.24)$$

where $\Delta\sigma$ is the spectral resolution ($1[\text{cm}^{-1}]$), and σ_{max} the maximum wave-number in the spectrum (1100 [nm]). Those parameters give a maximum angle of 0.01 [rad] or 0.57 [deg]. The α for our system can be calculated by knowing the entrance aperture (fiber core of 200 [μm]) and the focal distance of the collimating lens. The collimating lens was chosen of focal length equal to 12.6 [mm], this gives a beam diameter of

$$dia = f_t \tan \beta = 2.7[\text{mm}] \quad (4.25)$$

The maximum distance of the lens from the aperture is then calculated as follows

$$L_{max} = \frac{d}{\tan \alpha_{max}} = \frac{100[nm]}{\tan 0.01} = 0.01[m] = 10[mm] \quad (4.26)$$

where d is the half aperture, as shown in 4-17.

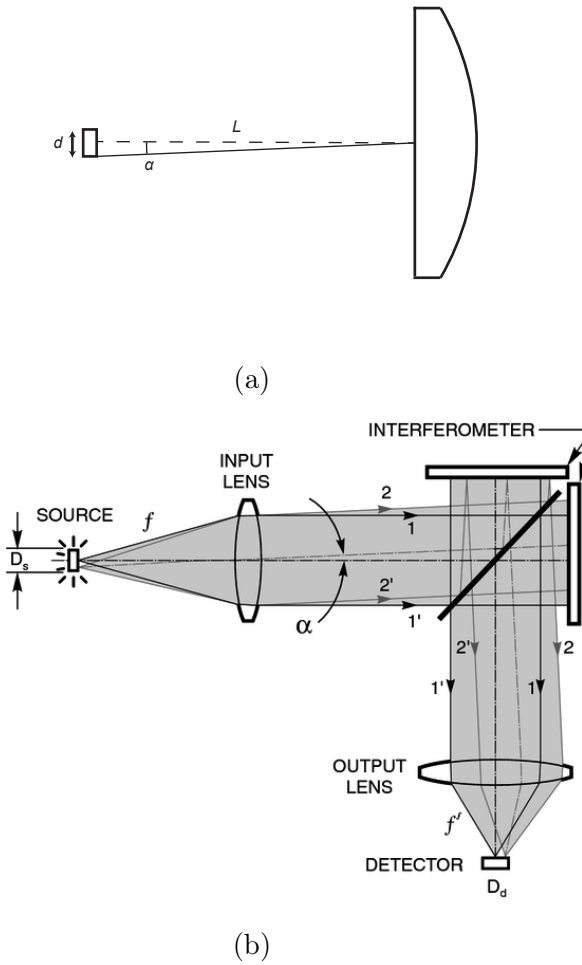


Figure 4-17: Role of the maximum acceptance angle α on the design of the Michelson interferometer, as explained in the text.

Chapter 5

Design of the chassis

All the optical elements, the fiber coupling optics, the Michelson interferometer and the dispersive optics will be accommodated in a compact structure. The structure, that is planned to be built from a bulk piece of aluminum, should allow a fine calibration of all the sensitive components, without losing its compactness. The mechanical chassis and the mechanical components needed were designed in SolidWorks. The collection of the Raman signal, excited by a 785 nm laser, is handled by a commercial Raman probe, (RPB785 from In-Photonics). The signal travels through a 200 [μm] optical fiber and is collected by a fiber coupler. It then enters the Michelson interferometer, and finally the dispersive part. The main part, the chassis, is shown in Figure 5-1. At the input is the fiber coupling and the collimating lens. The lens is mounted on a removable custom holder, designed for 0.5 [in] optics. A 2 DOF (degrees of freedom) mount holds the beamsplitter, allowing rotation and angle adjustments. The fixed mirror of the interferometer is mounted on a 3 DOF stage from Newport, allowing it to be tilted on two axis, and moved on the z axis. This is one of the smallest and less thick off the shelf mirror mounts available. The precise angle alignment is needed to achieve the highest dynamic range in the Michelson interferometer. A fixed mirror holder was designed to fit the moving stage, and it is shown in Figure 5-2. This mount was designed for the piezo linear stage and might need to be adjusted for other stages. After the

interferometer a curved mirror mounted on a 2 DOF stage focuses the beam on a pinhole, before entering the dispersive setup. The first curved mirror collimates the beam and steers it to the diffraction grating, that is installed on a rotating turret; this allows different groove density gratings to be installed, just by rotating the turret and thus illuminating the focusing mirror. Another advantage of the turret is to adjust for misalignment of the mirrors in the dispersive section since the mirror are fixed. Following the light path, finally a focusing mirror reflects the first mode from the grating to the CCD camera, that is externally mounted with a C-mount ring.

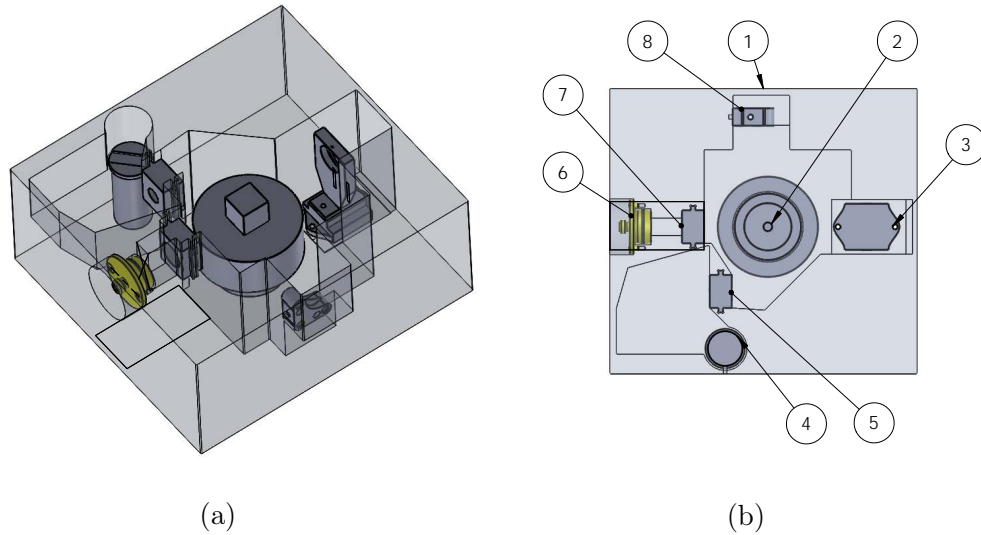


Figure 5-1: (a) Overview of the chassis and the components location. (b) Top view of the chassis. 1-the chassis; 2-the 2 DOF beamsplitter holder; 3-the translating stage; 4-the diffraction grating turret; 5-the pinhole holder; 6-the fiber input mount; 7-the collimating lens; 8-the fixed mirror

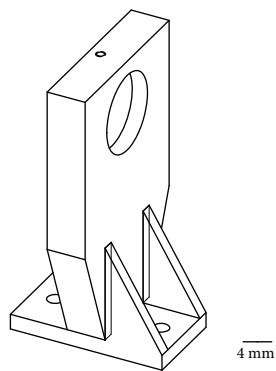


Figure 5-2: Design of the translating mirror holder, housing 0.5 [in] mirrors, to be placed on the top of the motion stage.

Chapter 6

Experimental results and data processing algorithms

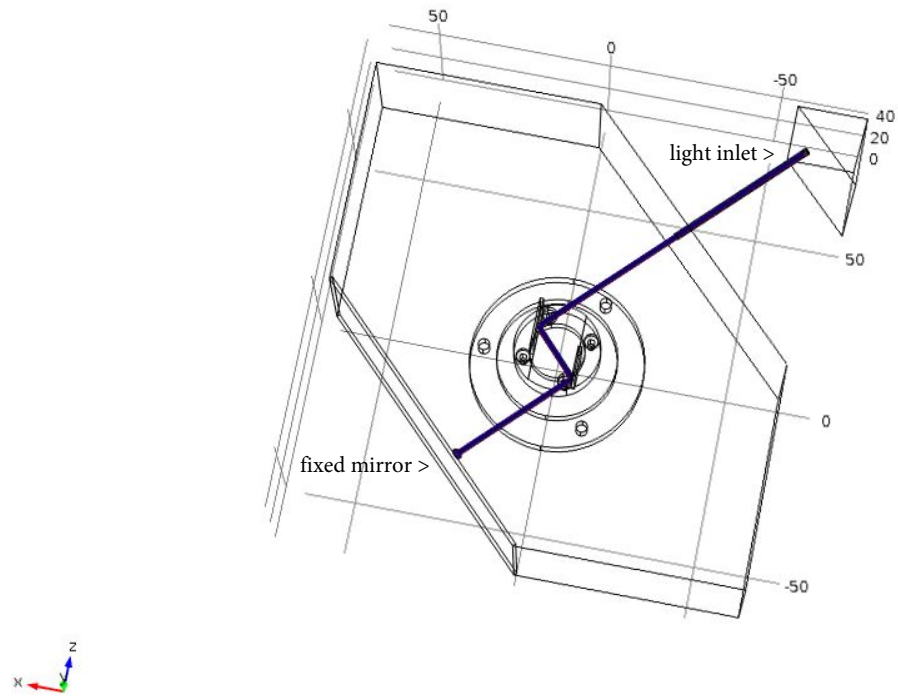
In this chapter the setup of the Michelson interferometer, and the three different configurations for the translating mirror will be presented: the rotating mirrors assembly, the piezomotor stage and the linear motor stage setup. The rotating mirrors have been assembled on a custom made platform spinned by a BLDC (Brushless DC) motor, for which an appropriate controller has been designed. The piezomotor, from PI, is a high resolution (up to 8 [nm] steps) linear motor, with a total span of 2 [cm], and a speed up to 2 [cm/s]. It can be operated both in single step modes or in linear mode. Its main disadvantage is the high vibrations at low speed. Finally the linear motor, from Thorlabs, is a linear single phase DC motor, that is coupled to a microposition optical stage by a precision screw. It can achieve very low speeds, but a reference laser, of a known wavelength, should be employed to have a very precise reference on the traveled distance. At the core of all the three experimented setups is a very performant CCD camera from Hamamatsu [17]; it is a 4 MPx camera capable of 20 Kfps on an area of 2048x8 pixels, and a quantum efficiency of more than 80%, possible because of its liquid cooling system that keeps the CCD at $-20\text{ }^{\circ}\text{C}$.

6.1 Rotating mirror setup

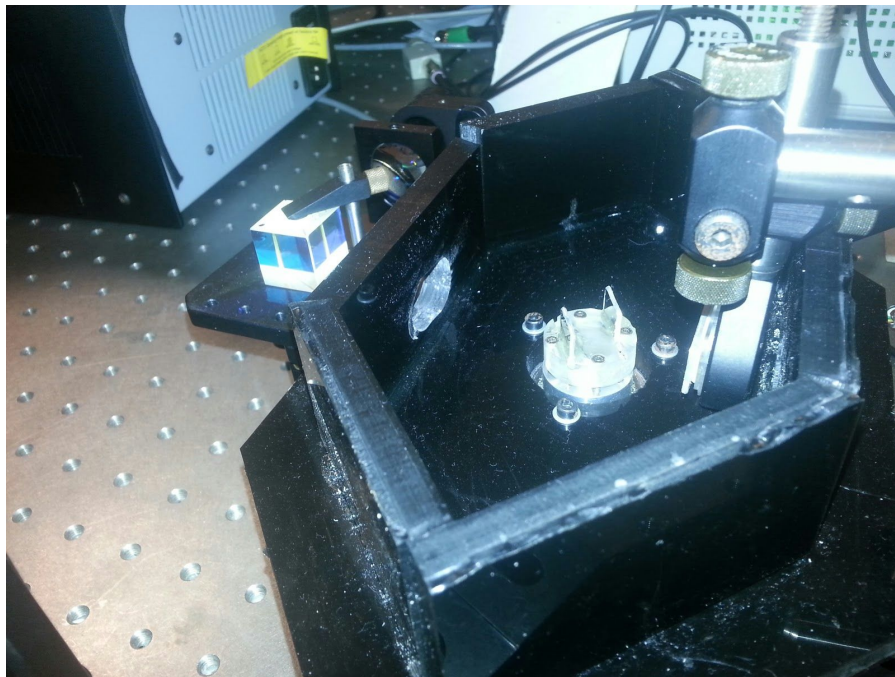
6.1.1 Rotating mirrors assembly

The core of this setup is a couple of mirrors placed face to face on a spinning wheel. The mirrors create a delay line of about 1 [cm] in the current configuration shown in Figure 6-1. The rays bouncing back from the rotating mount are redirected to the beamsplitter only for a portion of a complete turn of the wheel; the angle spanned in our configuration was computed using the ray tracing module of Comsol. Different configurations were analyzed, with mirrors of the same length or one shorter, and the optimal configuration was obtained iterating the simulation over a range of mirror's dimensions. In Figure 6-2 it is shown the achievable delay with two configurations where the mirror sizes are different. The angle spanned is larger in the first and optimal configuration, this allows a larger delay and hence an improved resolution. Mirror alignment, along with the reduced spanned angle, are the two main drawbacks of this configuration. From our interferometer simulations, described in Section 4.3 we observed that the maximum allowed angular error is of about 0.1 deg for each mirror in the horizontal and vertical plane. One big advantage over the linear motor is the stability of the rotor compared to the need to reverse the direction at every scan. We developed a stable and convenient control for a sensorless BLDC motor, described in the next section. The fact that a sensorless drive was employed allows us to have much more compact drives, that do not need any encoder, as opposed to the linear motion setup. Finally we estimated the required sampling frequency and discovered that very high sample rates are required: in the case of a 2 Hz speed (needed to achieve a minimum stability for the motor) and a total scan of 2 cm, occurring for only 20 degrees of the complete rotation, we need to sample the complete run in 1/9 of seconds. In order to detect 632 [nm], according to the Nyquist sampling theorem, we need to collect samples at least every 150 [nm] which makes 4 samples per wavelength. For a length of 2 [cm], we have to

collect 133333 samples in $(1/9)$ seconds. This means that the speed required is $9 \cdot 133333 = 1.2$ MHz. According to these calculations, we need a CCD setup that is capable of recording at 1.2 MHz. Nevertheless an interferometer was set up to test the idea, and instead of the CCD camera, a photodetector was employed to record the interference signal. A sample spectrum obtained with this setup is shown in Figure 6-3, for a red LED light, and a red LED plus a 825 [nm] laser as reference.



(a)



(b)

Figure 6-1: (a) The light travels through the mirrors assembly that creates a delay of 13 [mm] in this configuration. A shorter mirror is mounted to allow a longer scanning range. (b) The assembled setup is created from machined ABS plastic: the manufactured rotating stage is composed by the spinning mirrors mounted on a BLDC motor, the fixed mirror on the right and the inlet hole on the left.

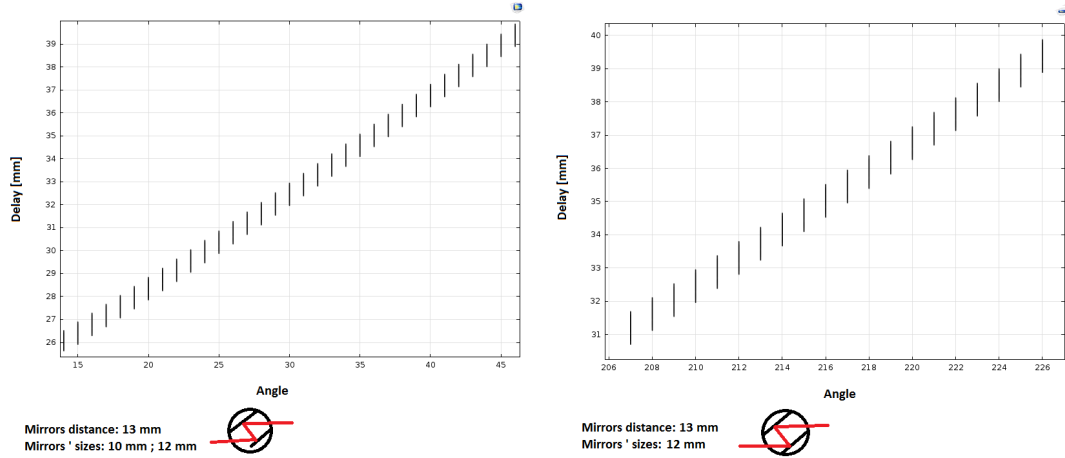


Figure 6-2: Delays obtained for two simulations. X axis is the discrete time intervals where ray propagation is performed, Y axis is the absolute delay in mm. In the first plot a shorter mirror is employed, while in the second plot two mirrors of the same length are mounted.

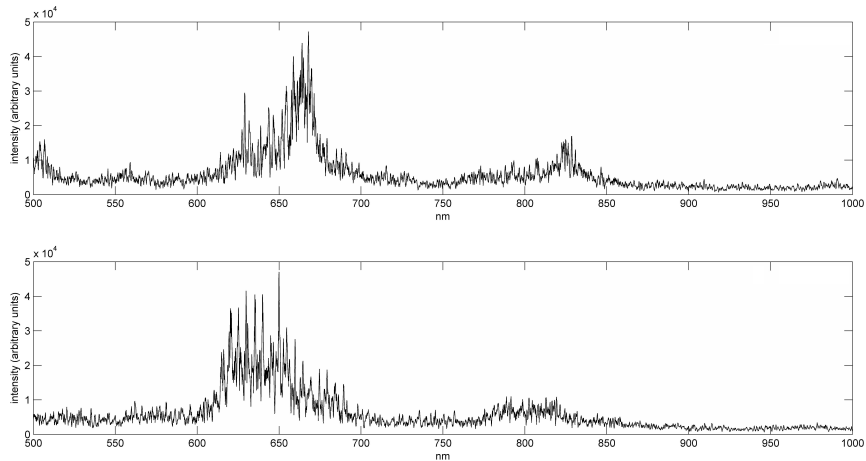


Figure 6-3: Raman spectrum obtained from acetone sample, and the background noise in the second plot.

6.1.2 Sliding mode control

In this section the control algorithm and implementation of the BLDC motor, that spins the rotating mirror stage is presented. Compared to a single phase motor, such as the one from Thorlabs that we employed in the third and final setup, it presents a much more complex architecture. In fact a single

phase motor can be controlled with a simple servo loop, and an outer speed and position loop, each one with its own PID control. The speed and position feedbacks have to be taken from an external encoder, or a reference laser in the case it is employed in an interferometer. The BLDC motor has the possibility to collect the speed signal from the same windings that are used to drive it, but a much more complicated control algorithm has to be developed.

BLDC motors driving principles BLDC motors, consisting in $3n$ pairs of winding where n is the number of poles, can be controlled giving three sine waves 120 deg apart to the windings, placed in a star configuration. If we consider the frame of reference of the stator with respect to the fixed axis, as shown in Figure 6-4, the first transformation is known as the inverse Clarke transformation, from the frame of reference abc to $alpha - beta$: it converts the three balanced currents in the three-phase stator frame into two phase-balanced currents in an orthogonal stationary frame. This occurs in the same plane as the stator frame, but the angle between the two axes is 90 degrees instead of 120 degrees. The second transformation from the frame $alpha - beta$ to dq is called inverse Park transformation. It transfers the stationary frame to the rotor frame to make the AC currents into DC currents [18].

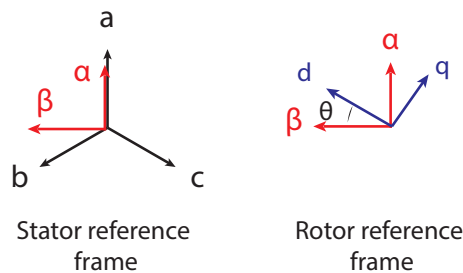


Figure 6-4: Clarke, on the left, and Park, on the right transforms.

Control design and simulation Control design was implemented in Simulink, and can be seen in Figure 6-5; the specifications were very relaxed, but a requirement was to be a sensorless drive with very little speed oscillations. Speed

requirements were ranging between 50 to 100 rpm. The system is composed by a block named “palnt” that implements the motor simulator and the bridge, it is backward connected to a Clarke and vectorial pwm generator, that takes as input the alpha and beta components from the inverse Park transform. The inverse Park transform is fed by the current angle of the rotor, θ , and the PID control signals for the I_d and I_q current components. I_d reference is set to 0 because its field is aligned with the rotor magnet, and thus not giving any torque, while the I_q reference component comes from the outer speed loop. The plant was tested first taking the reference from the motor block and directly feeding it to the PID controllers, bypassing the observer. This allowed a first rough tuning of the PID controllers.

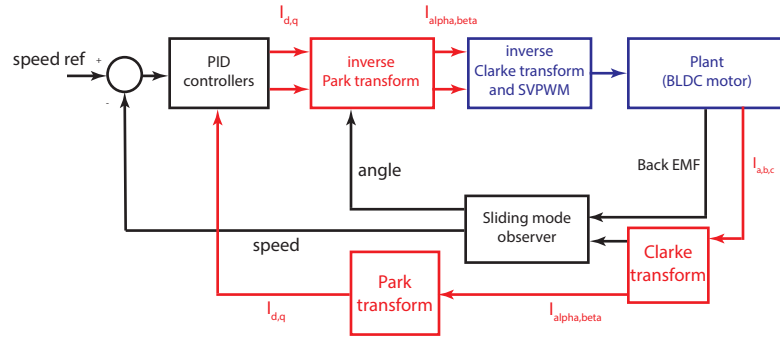


Figure 6-5: Schematics of the sliding mode control as explained in the text. The red blocks are the inner current loops, closed directly on the current feedback of the motor. The outer black loop is the speed control, closed through the sliding mode observer, instead of the encoder data that would be seen on traditional PID controls.

Sliding mode observer design and simulation The sliding mode observer was designed in order to estimate speed and angle of the rotor from the alpha and beta measured currents and voltages. It is composed by a flux and current observer, a signum function, a low pass filter and a Back EMF modified observer. The estimated (from the voltages) alpha and beta currents are compared in the first block and the sliding surfaces are $L_d * I_d$ and $L_q * I_q$.

A complete report on the existence of the sliding conditions is given in [19]. The block diagram of the sliding mode observer in a detailed form is shown in Figure 6-6. Flux/current observer and modified back EMF observer are connected in cascade. Low pass filtering the signals is essential, and needs a very fine tuning to ensure good accuracy. The results from the sliding mode observer were compared with the velocity profile obtained in the previous simulations, for a well characterized motor. The two profiles are given in Figure 6-7. A bootstrap block has been also added to allow the rotor to be aligned with the flux and start rotating. This block also implements a ramp function that drives the motor close to the desired speed in open loop mode.

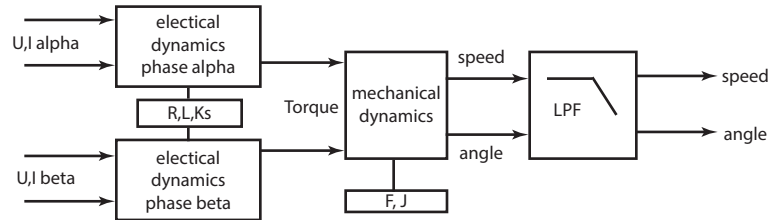


Figure 6-6: The sliding mode observer takes as input the voltages and currents from the Park transform, and simulates the operation of a drive. The first part is the electrical dynamics, where the resistance R and the inductance L of the coils are considered. The second part, linked to the first one by the machine constant K_s , emulates the mechanical dynamics, taking into consideration the friction F and the inertia J . Angle and speed signals are the output, and low pass filtered to ensure smoothness for the next steps.

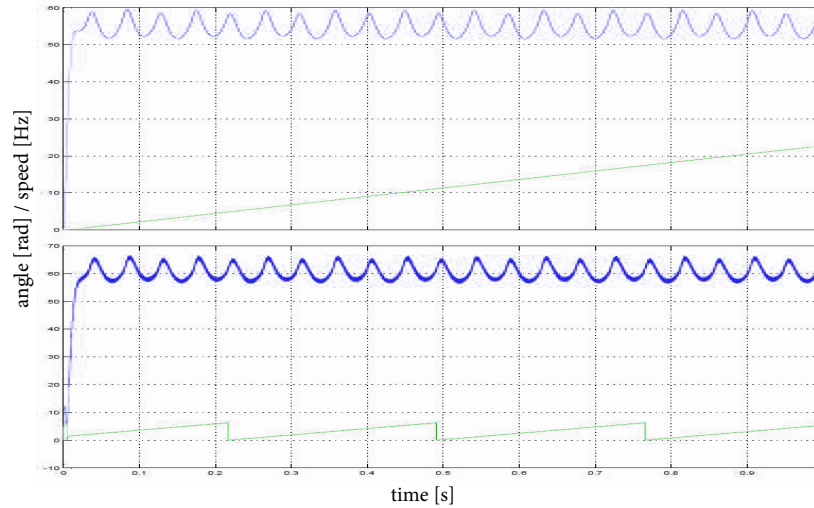


Figure 6-7: First plot is the reference speed (blue) and angle (green) from the plant, and second one from the sliding mode observer. Speeds and angle slopes are in good agreement.

6.2 Piezomotor implementation

In this implementation a piezomotor translating stage was employed to displace the moving mirror of the interferometer and to record the interferogram. The stage is shown in Figure 6-8, and a 0.5 [in] mirror mount is directly mounted on the top of it. The design of the algorithm to sample the interferograms presents multiple challenges: first the synchronization between the camera and the motion stage should be achieved, the snapshots taken by the camera and the position of the mirror should be correlated. Then, at a later stage, the speed of the whole scan should be optimized, and that proved to be the most challenging issue to solve. The camera is interfaced to the computer through a CameraLink interface, which allows acquisition speed up to 10 KHz for an area of 2048x8 pixels. A Matlab toolbox allows the acquisition of the images directly into the software, for later processing. The triggering can be both internal, allowing an output trigger for synchronization, or external. The motion stage has a movement accuracy of 8 [nm], allowing very fine movements. Its controller can work in either open loop or closed loop modes, the later being obviously much slower. The controller also allows external or

internal trigger, having a set of commands that can be used to create macros for customized behavior. The interferometer we set up to test the two devices is shown in Figure 6-9: a 632.8 [nm] laser beam is expanded and attenuated, on the bottom is the fixed mirror, on the right the moving mirror and on the top the CCD camera.



Figure 6-8: The PI motion stage used in this setup.

In a first approach we scanned at a 100 [nm] rate, in closed loop configuration, to achieve the highest accuracy, the output trigger from the controller was used to trigger the camera. This allows having the highest accuracy possible, but at the cost of a very slow scanning speed: each step takes about 80 us (the instructions speed of the controller is 8 us, and about 10 instructions are processed for each motion command). At this rate 1 cm takes 800 seconds to scan. A second approach was to run both the camera and the piezo drive in free running mode: the camera takes images at the highest rate possible, and the controller moves the stage at a pseudo constant speed. The piezo motor works by translating the stage of finite steps, defined by the amplitude of the pulse sent to the piezo. Since the stage has an optical encoder, the controller can be programmed to output a trigger signal every fixed traveled range. The acquisition of an interferogram follows this flow: the camera interface software is set to record a fixed number of images, say 150000, at a speed of 12 KHz for a total time of about 12 seconds, and export an AVI file with all the images acquired. The images are a 8x8 pixels square of 64x64 [μm^2] centered on the

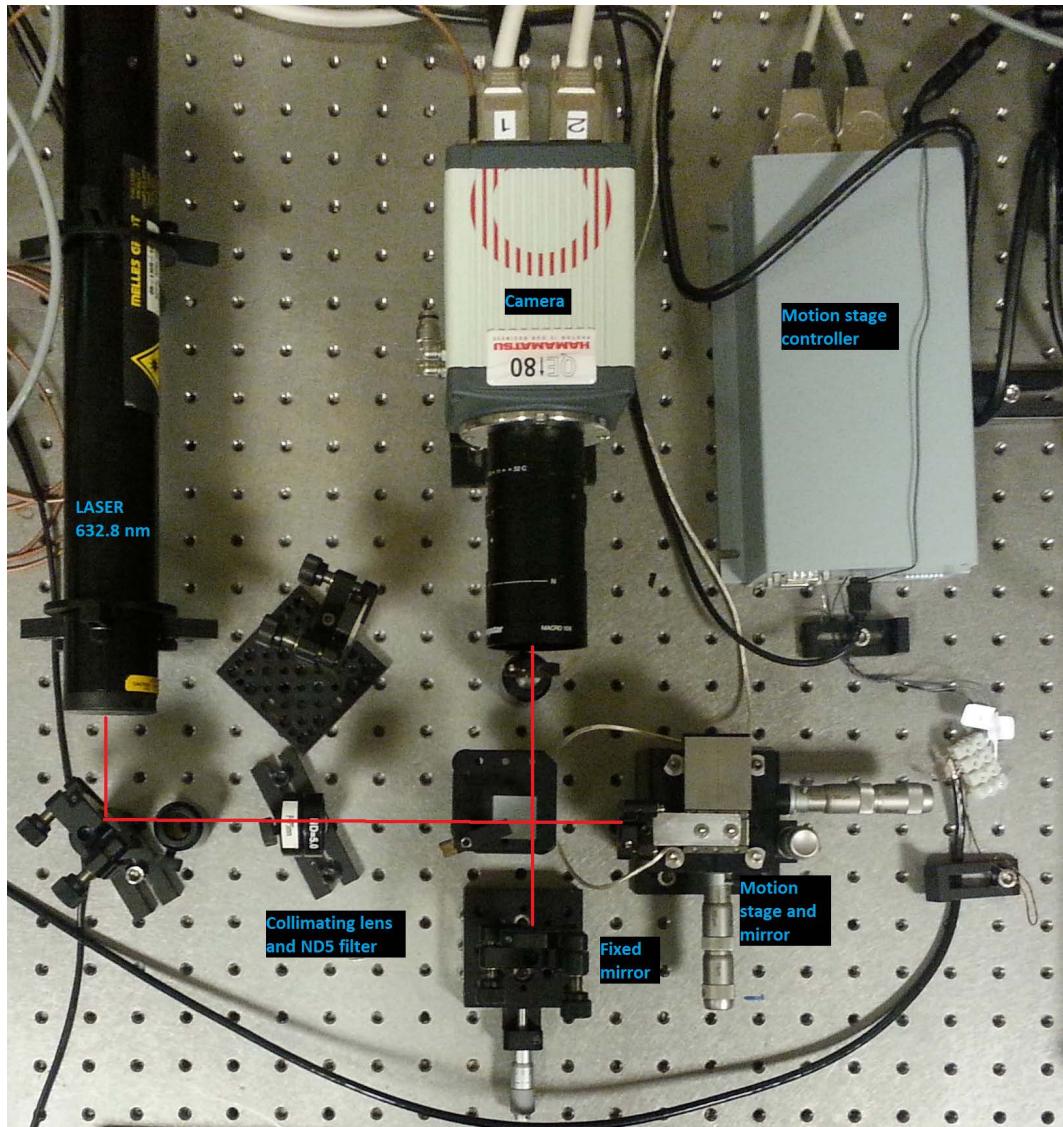


Figure 6-9: The interferometer setup as described in the text.

beam. While the camera acquires the images, the motion stage moves at a constant speed. In the meantime a NI acquisition board records the camera triggers, the motion stage $5\ \mu\text{m}$ trigger signal and the global trigger that starts both the camera and the motion stage. This flowchart and the timing diagram are shown in Figure 6-10 and 6-11.

Having the camera firing trigger and the controller steps, a non uniform sampling scheme can be used to take the Fourier transform of the acquired data points from the camera, even if the spacing between them is not uniform.

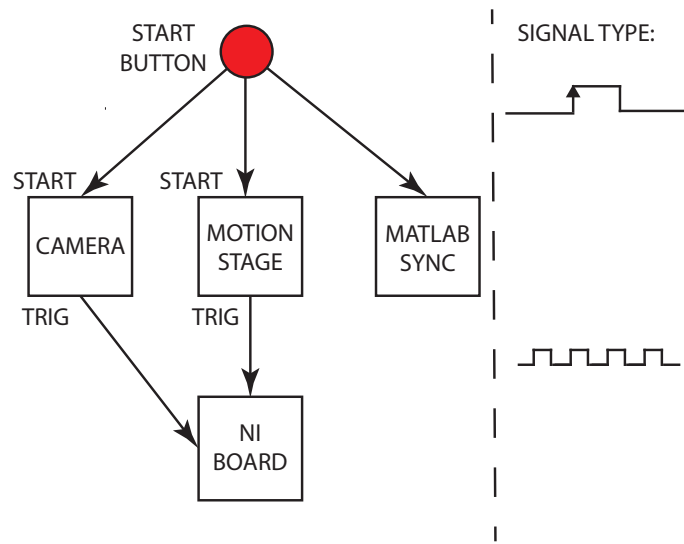


Figure 6-10: Schematics of the data acquisition process: the start button issues a global trigger to the motion stage and to the camera; it is also collected by the acquisition board. The acquisition board records the triggers from the camera and from the motion stage.

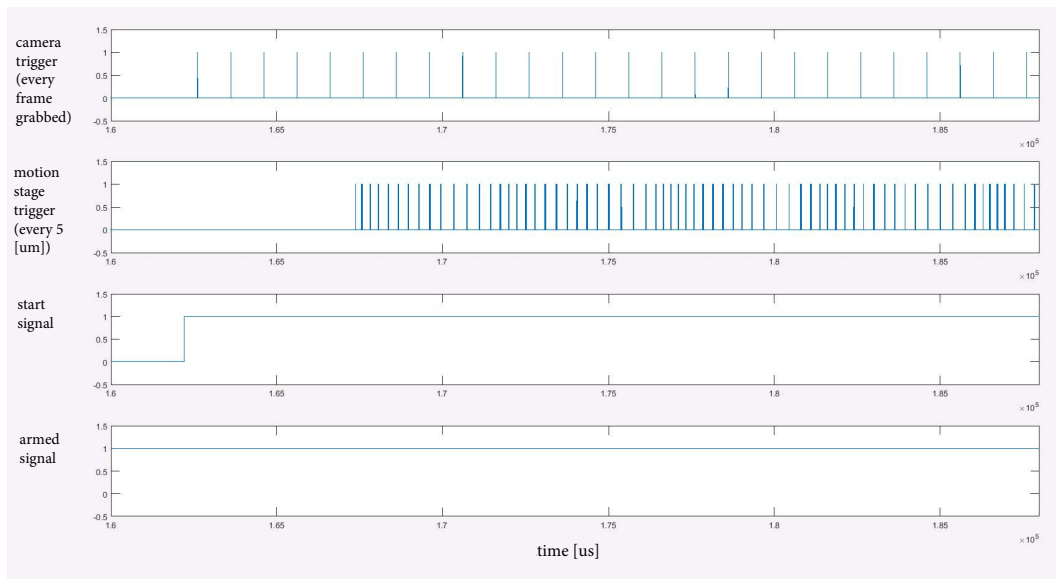


Figure 6-11: This is the timings chart of the signals recorded on the acquisition board: the first signal is the camera trigger, occurring at a constant rate; the second signal is the motion stage trigger, they are uniform in space ($5 \mu\text{m}$ apart), but not uniform in time. The third signal is the start trigger, and the last signal is a convenience switch to start the data acquisition in Matlab.

The algorithm developed takes care of the nonlinearities of the piezoelectric motion stage. The stage is programmed to output a trigger signal every 5 $[\mu\text{m}]$, a distance that is adjustable, but should be chosen accordingly to the stage speed to fully resolve the different trigger peaks. The camera outputs a similar trigger signal every picture taken. The stage trigger is then uniform in space, but the camera trigger is uniform in time. To be able to take the Fourier transform of the intensities, it is necessary to first assign to every image a traveled relative distance. This is done by knowing both the 5 $[\mu\text{m}]$ steps time (the rising edges) and the time each frame has been captured. With these information an interpolation is performed on the camera signal where, between the 5 $[\mu\text{m}]$ steps, the motor is assumed to have a linear motion (other interpolation methods have no effect on the overall performance of the algorithm). It is here necessary to filter the data because of the bouncing effect of the optical encoder in the motion stage: as shown in Figure 6-12 when the stage moves a step it oscillates around that position, and produces fake 5 $[\mu\text{m}]$ trigger signals. This has been filtered out by setting a time threshold, equivalent to 10 clock cycles of the controller (80 $[\mu\text{s}]$). After the interpolation array has been constructed (a portion of a sample interpolated array is shown in Figure 6-13), the multiple frames grabbed by the camera are averaged and a nonlinear discrete Fourier transform (DFT) is applied to the data, where to each intensity it is associated a relative distance from the starting point. Fast Fourier Transform (FFT) can not perform well in this context, and some degree of interpolation is needed to fill in gaps. An alternative is the Lomb-Scargle method (or least-squares spectral analysis, LSSA), which estimates a frequency spectrum based on a least squares fit of sinusoid [20]. The Lomb periodogram is used when incomplete or unevenly sampled time series of data are available. Spectrum of laser signals and of broadband light were taken, but we noticed that the vibration of the piezomotor had negative effects on the acquired signal, due to the nature of the moving mechanism: small piezoelectric elements move a linear stage by hitting the sliding rod at a constant frequency, as shown in

Figure 6-14. If at high driving frequencies, namely above 20 KHz, the effect of such a vibration is neglectable, at lower frequencies it is well noticeable. A comparison of the spectrum of a red LED at different driving frequencies is shown in Figure 6-15c, and the spectrum of a 785 [nm] laser, taken at the driving speed of 25 KHz is shown in Figure 6-16. Even though at high frequencies it is possible to obtain a quite clear spectrum, our camera can not follow such a speed as shown below:

the stage speed was measured experimentally at 25 KHz driving frequency, and it turned out to be 0.02 [m/s]. To have a minimal detectable wavelength of 400 [nm] we need steps size of 100 [nm], that means a sampling frequency of:

$$0.02 \text{ [m/s]} / 100 \text{ [nm]} = 200 \text{ [KHz]}$$

But our camera has capabilities of recording only at about 15 KHz on an area of 2048x8 pixels. The results where the piezo driving frequency was above 5 [KHz] were taken employing a photodetector instead of the camera, working at a sampling rate of 1 MHz.

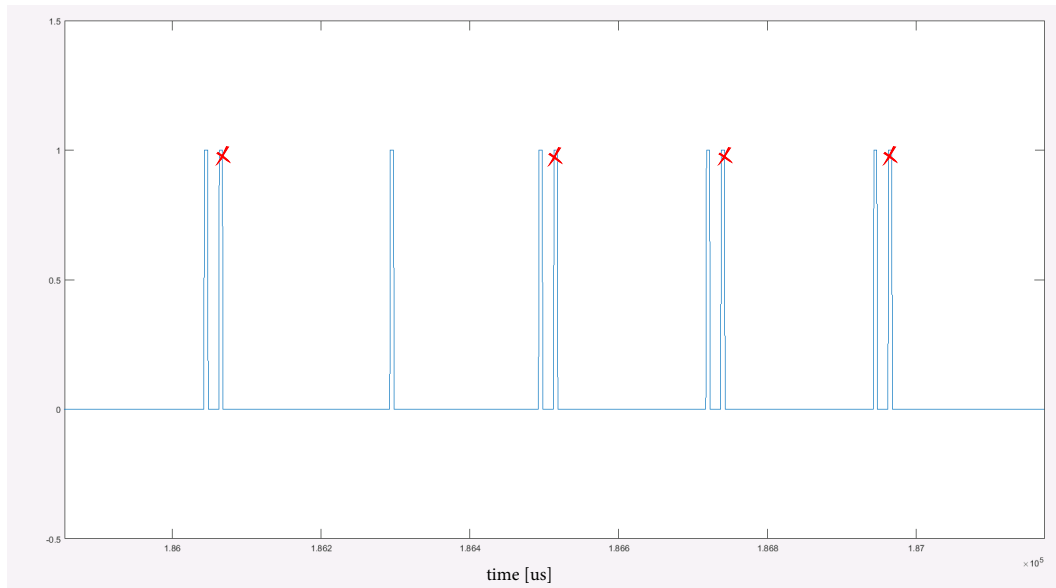


Figure 6-12: Bouncing effect on the micropositioner signal, the spurious edges are marked with a red cross.

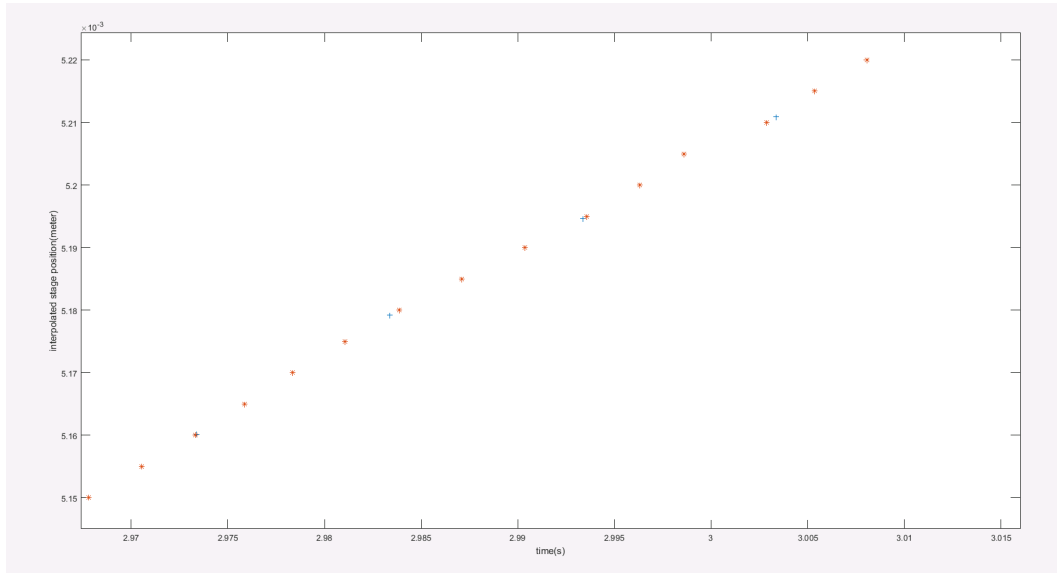


Figure 6-13: The interpolated data: points marked with a + are the actual rising edges of the stage triggers, while the points marked with * are the interpolated data.

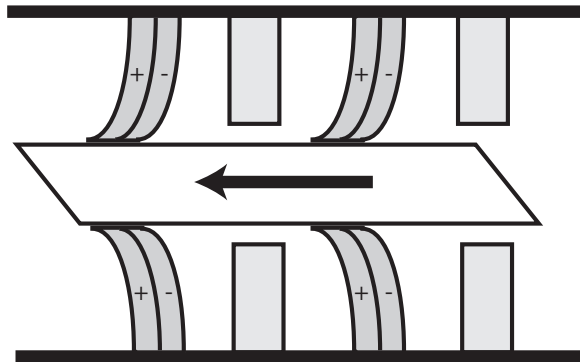
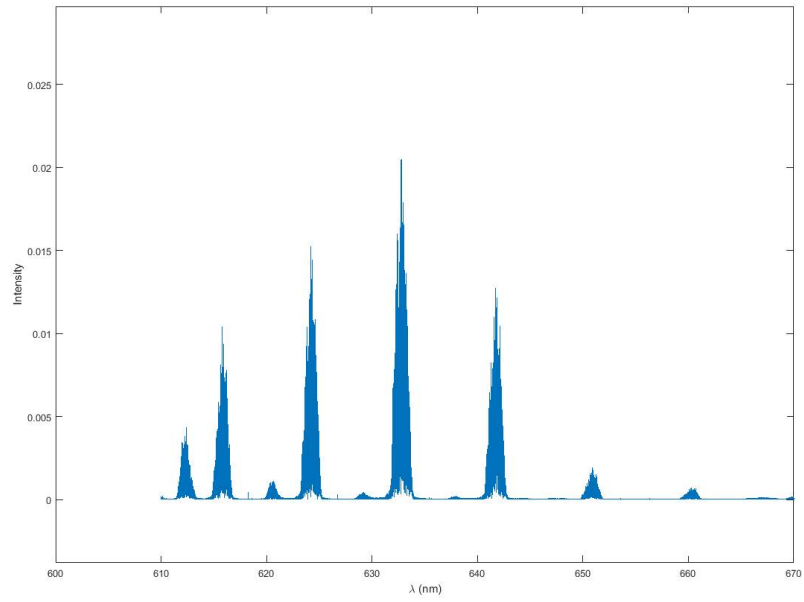
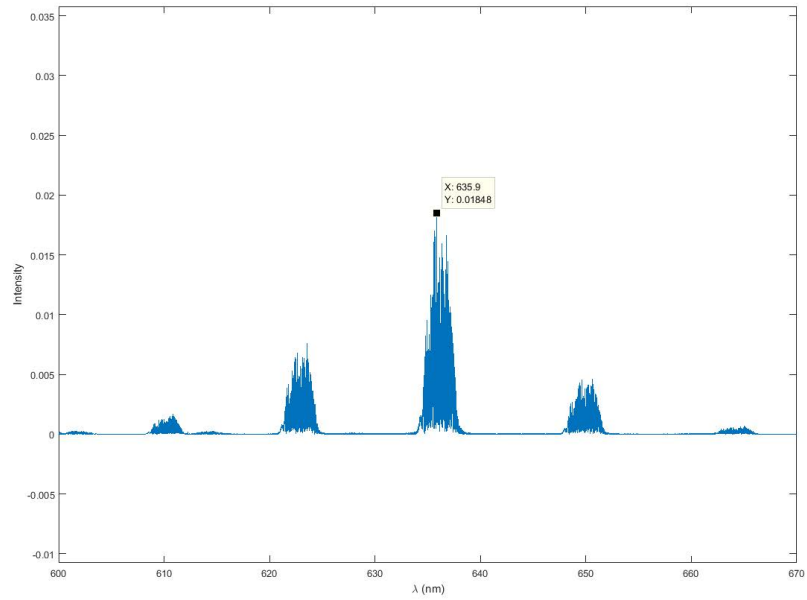


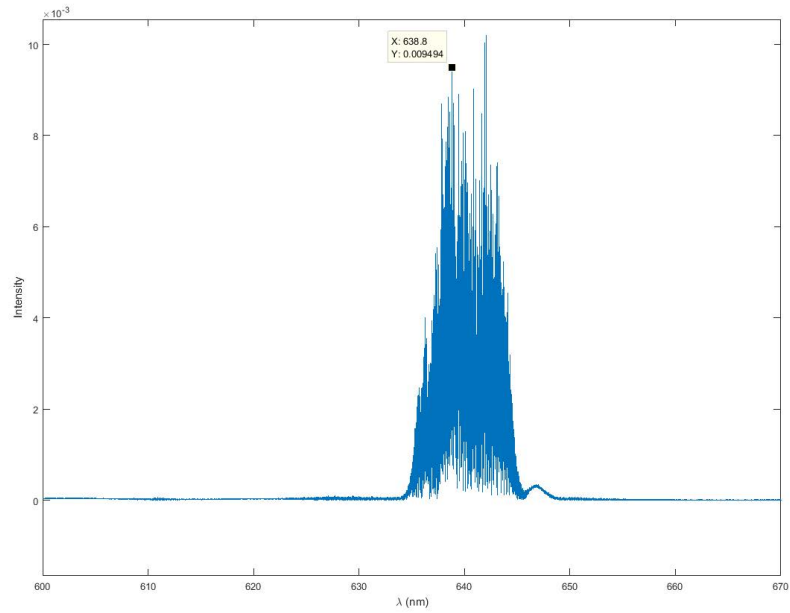
Figure 6-14: Simplified schematic of a linear stage driven by a piezo motor: the PZT elements (gray) are fired alternatively at a constant frequency to translate the stage.



(a)



(b)



(c)

Figure 6-15: Three red LED light spectrums acquired with the piezo motor setup. (a) is acquired with a driving frequency of the stage of 10 KHz, (b) at 20 KHz and (c) at 25 KHz. The side bands are possibly due to the vibration of the stage that is acting as a modulation on the acquired signal.

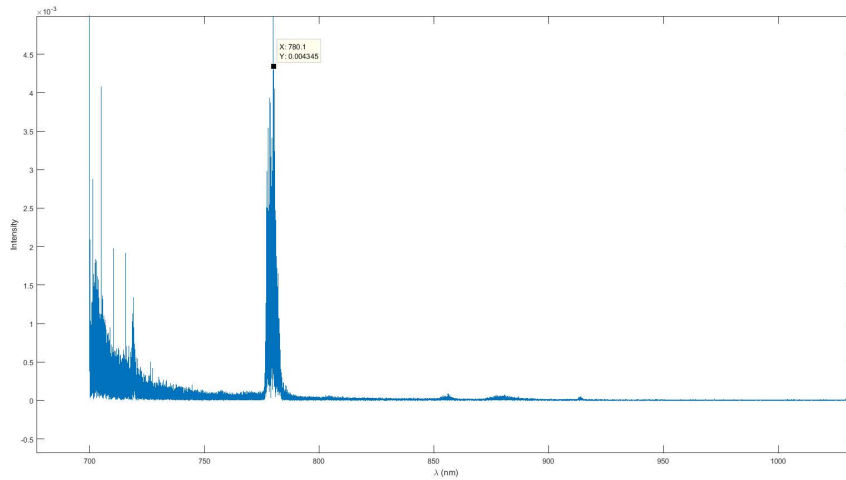


Figure 6-16: Spectrum of a 785 [nm] laser acquired with a driving frequency of the stage of 25 KHz. The effect of the vibration of the stage is noticeable in the quite broad spectrum of the peak (about 15 [nm]).

6.3 Linear motor experiments

Here a linear motor is employed to translate the moving mirror, the motor is a single phase DC motor from Thorlabs (P/N Z612B). In this configuration the motor is driven in open loop and an auxiliary He-Ne laser is employed to find the traveled distance. The configuration, shown in Figure 6-17, have two beams traveling different paths, the main beam, the blue one, carries the signal we want to analyze, while the red one is the reference beam. The interference of the reference beam is used to find the distance traveled by counting the number of points at which the signal crosses the zero axis, in fact since the laser wavelength is 638.2 [nm], the intersection will occur every 160 [nm] roughly. This information is used to compensate for the non uniformity of the motor speed, following the same algorithm we employed with the piezo motor stage: the zero crossing points, occurring every 160 [nm] will play the role of the trigger signal spaced 5 [μm], coming from the motion stage. The obtained zero crossing points, shown in Figure 6-19, are used to interpolate the camera trigger signal, and assign to every image a traveled distance.

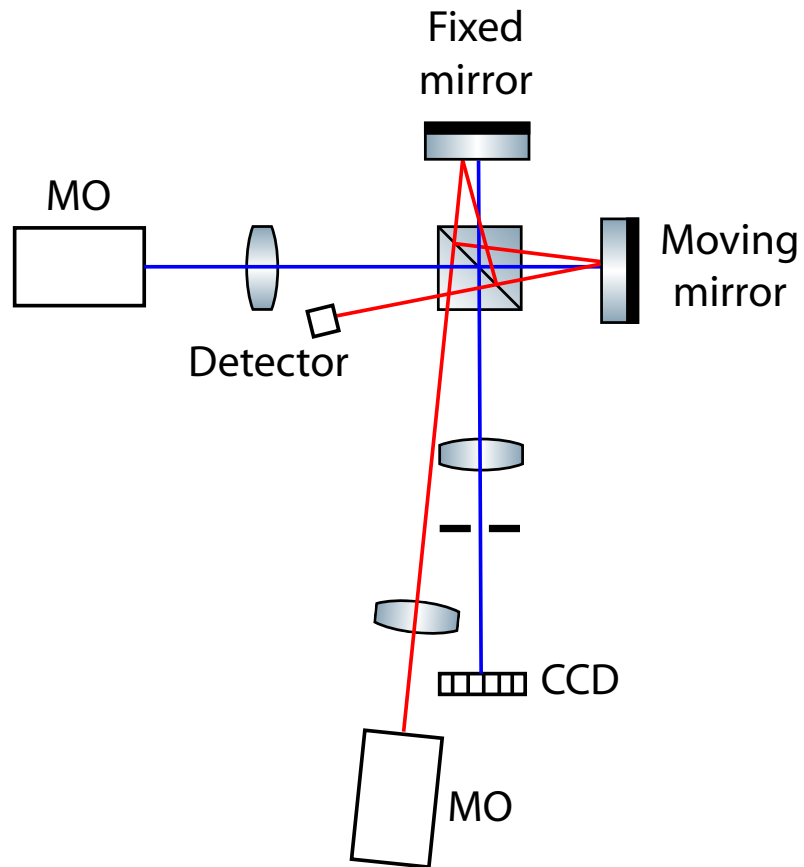


Figure 6-17: Interferometer schematics: the blue light path is the main beam, it is expanded by a microscope objective, collimated, and sent through the interferometer, falling afterward on the CCD camera. The red path is the reference beam, it follows the opposite path of the main beam.

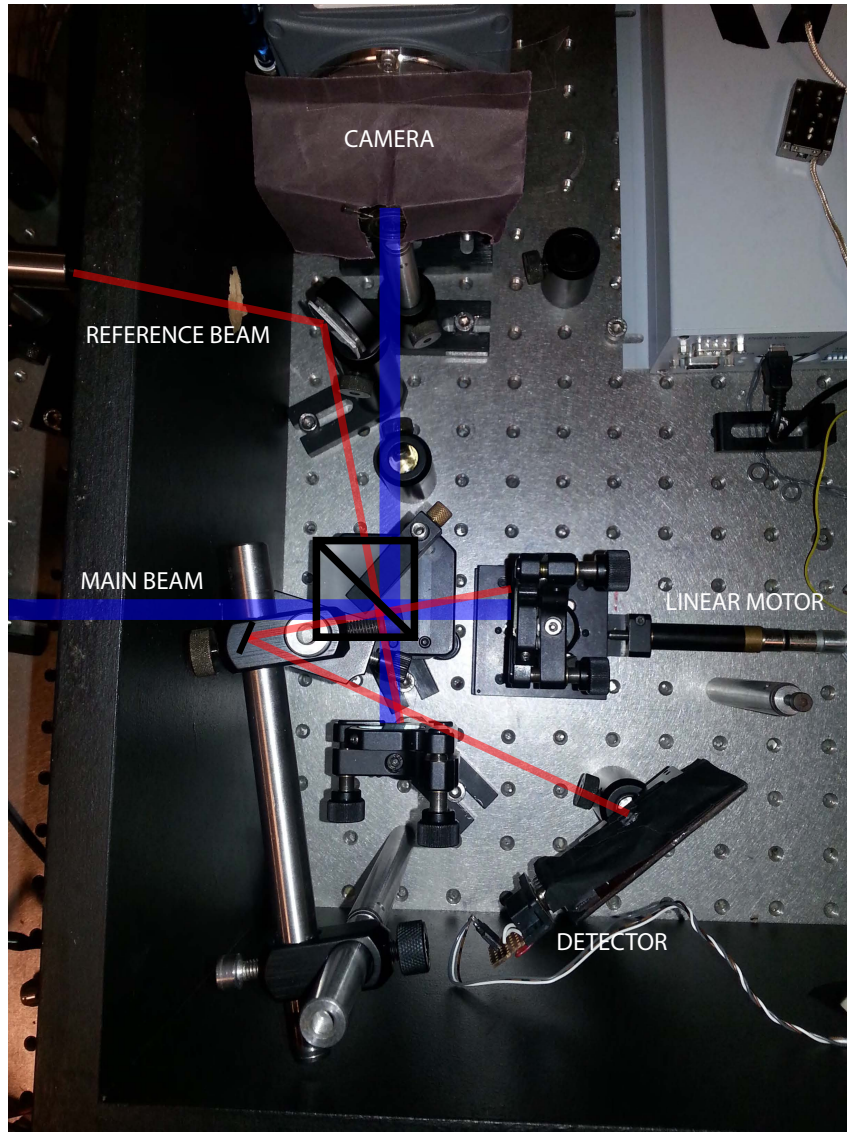


Figure 6-18: Picture of the interferometer with the main (blue) and reference (red) beams.

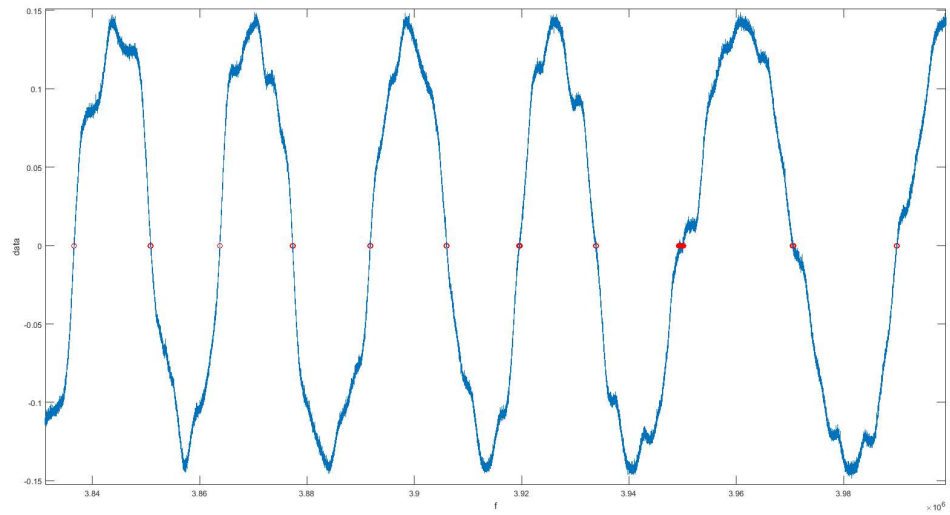


Figure 6-19: A few cycles of the reference beam interference, with the zero crossing points marked with orange circles.

A good alignment of the mirrors was essential in this setup, since both the beams, the reference and the main beam had to overlap to create the interference. To achieve this a 785 [nm] fiber coupled laser was used: the laser was employed below the threshold level not to saturate the camera and to image the fiber mode shape, displayed in Figure 6-20. Since the mode has the dimensions of few micrometers, comparable to the multimode fiber core size, overlapping the beam coming from the two arms of the interferometer led us to a very high contrast interference. This made much more easy to record the interference of a broadband signal. An example of the interference for such a signal is shown on Figure 6-21, for an Halogen lamp.



Figure 6-20: Image of the fiber mode acquired by the camera, used to perfectly align the two interferometer arms.

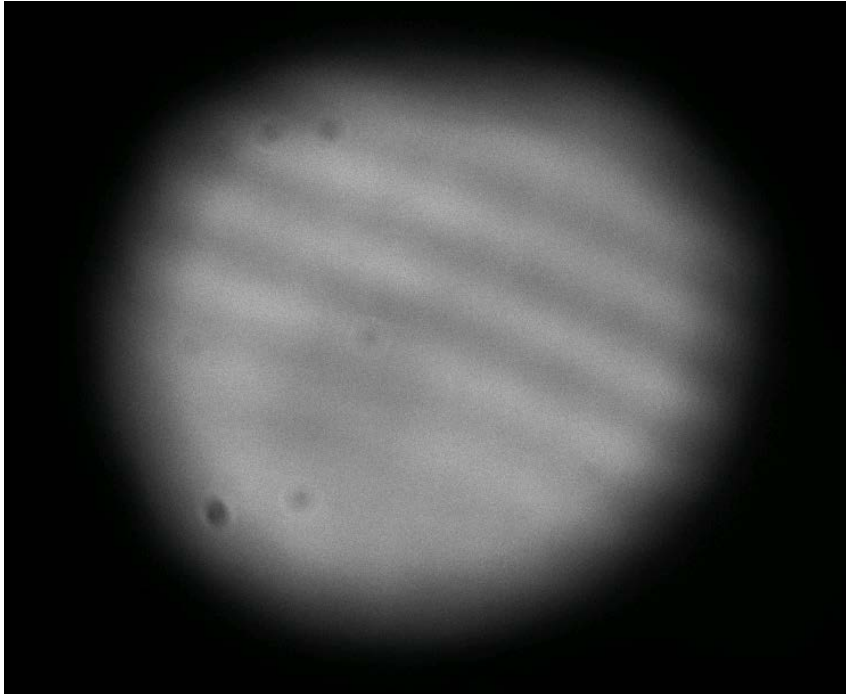
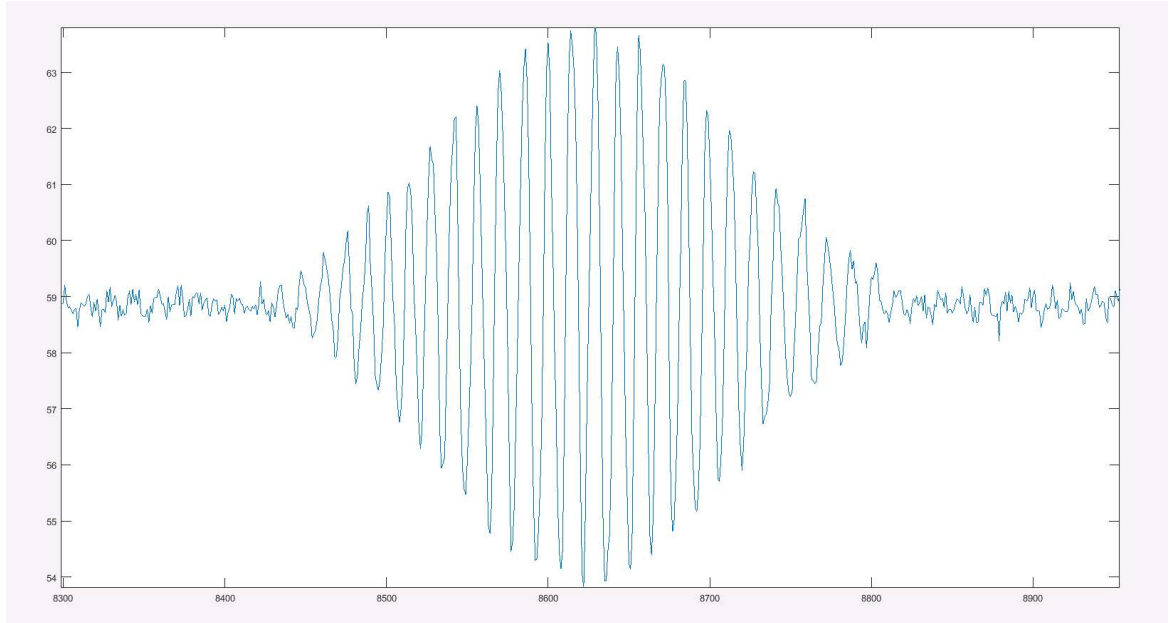
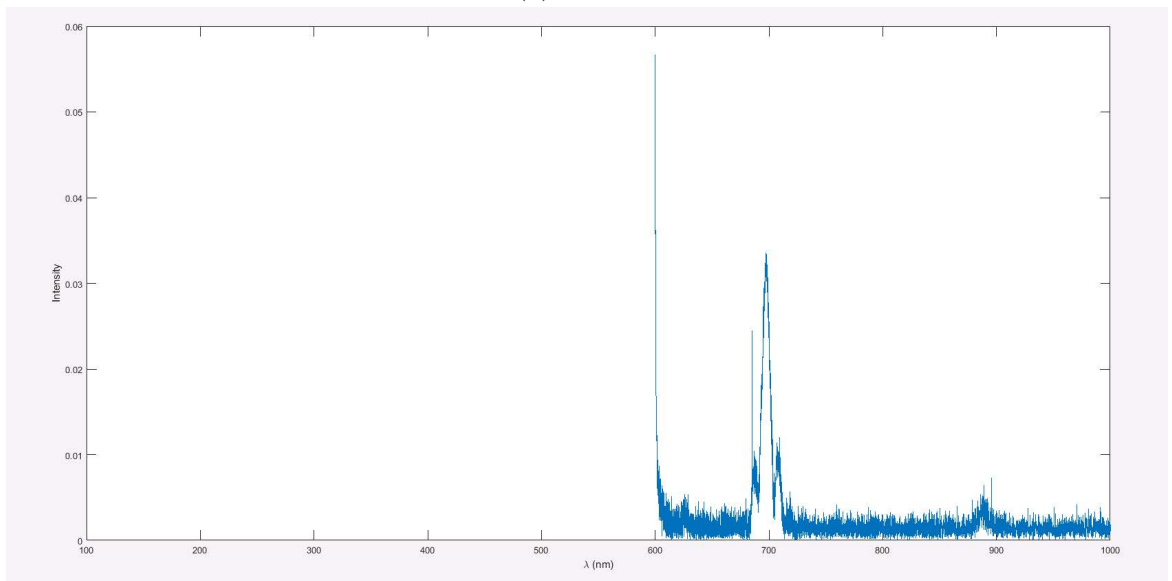


Figure 6-21: White light spectrum interference recorded with the camera. The interference occurs at the point where the interferometer arms have the same length.

We recorded successfully spectrums of different light sources. The algorithm used for the piezo motor stage has been adapted to this new configuration where instead of the triggers from the motion stage, the signal coming from the interference of the reference laser on a photodetector was employed to find the zero crossing points and interpolate the camera triggers. Spectrum for IR led and yellow led were recorded by letting the motor travel for a distance of 3 [mm] around the point where the interferometer arms have the same length, and where the interference occurs. The FT of the time signal was taken employing the same Lomb algorithm described for the piezo motor experiments, but in this case the intensities location was taken interpolating the zero crossing points of the reference beam. In Figure 6-22 and 6-23 the interference and the corrected FT are displayed for the IR and yellow leds.

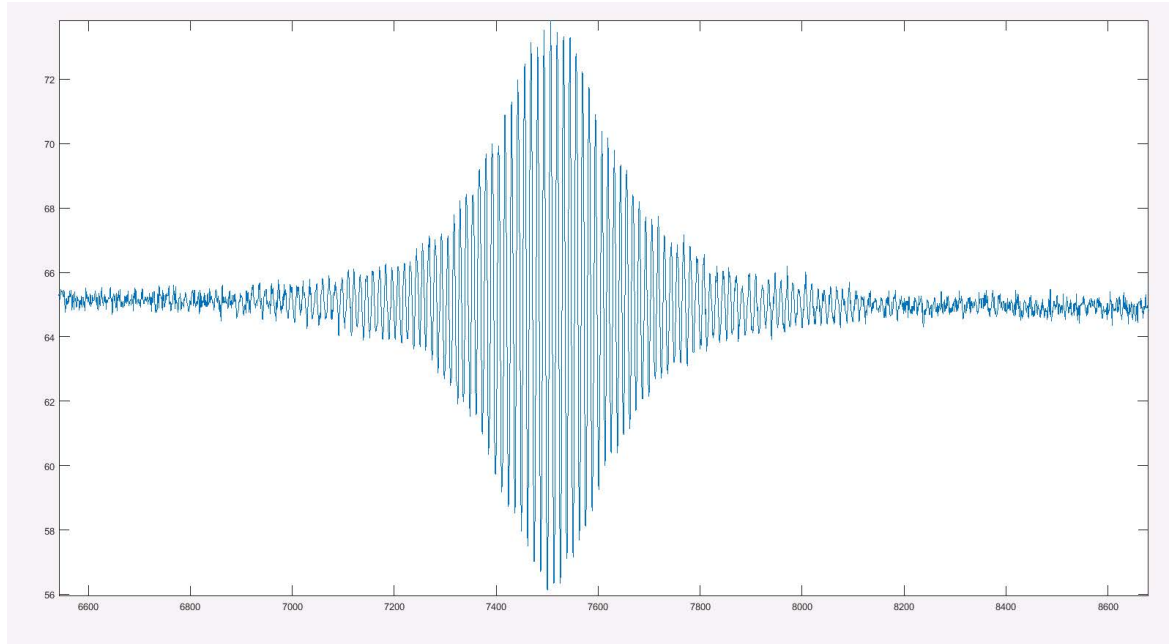


(a)

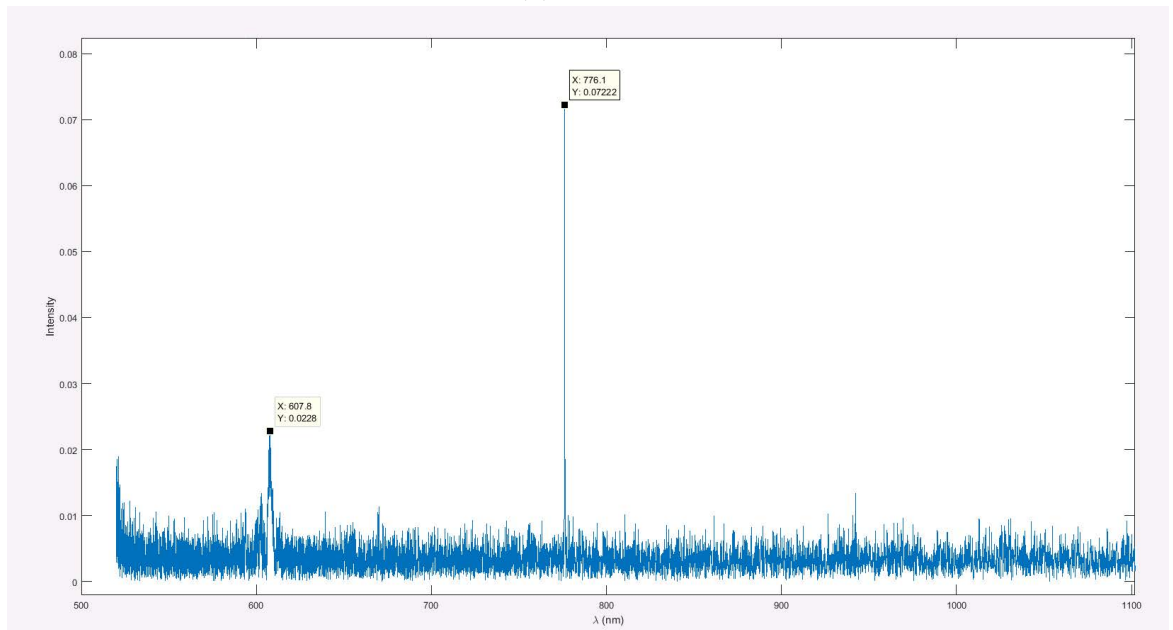


(b)

Figure 6-22: Time signal and its corrected Fourier transform for an infrared LED.



(a)



(b)

Figure 6-23: Time signal and its corrected Fourier transform for a yellow LED with a 785 [nm] laser light superimposed.

Chapter 7

Conclusions and future works

In this thesis a novel design for a hybrid spectrometer is proposed, the advantages of such a system are the reduced fluorescence effect with respect to traditional FTIR spectrometers, since the wavelengths are not all detected by a single photodetector, but by a CCD array. This will allow the spectrometer to work at higher excitation wavelengths, allowing a better signal to noise ratio. The system is composed by three main parts, the signal collection optics, the interferometer and the dispersive optics. Many challenges have been encountered in the design of the dispersive and FTIR parts: the aberrations cause a loss of signal in the Czerny-Turner configuration, and it is necessary to correct for them, the CCD detector position has to be finely tuned to achieve the best signal to noise ratio. The interferometer has also to be carefully designed since tiny misalignment in the optics cause high power loss in the signal. The input fibre coupling optics are also a sensitive component since the acceptance angle of the interferometer is very narrow. Finally a mechanical chassis has been designed trying not to neglect any of the multiple hints obtained from the simulation of all the components. Subsequently the interferometer has been set up to test three different motion solutions for the translating mirror: a rotating mirror assembly, a translating piezomotor stage and a linear single phase motor. The main issue has been to find a good compromise between the minimum achievable speed of the stage to keep a certain stability, but at

the same time a speed that would allow the CCD camera, with a much lower sampling rate than a photodetector, to sample at least 100 [nm] steps, needed to detect a 400 [nm] wavelength. The best choice turned out to be the linear motor, that has the better stability at low speed.

In this thesis work both the dispersive and interferometer sections has been designed and simulated, but only the interferometer has been built and tested. In a future work the complete system will be set up, following the guidelines in this thesis; the whole system, composed by the interferometer and the dispersive optics will be tested and assembled in the chassis proposed, with minor revisions to accommodate a specific motion stage.

Bibliography

- [1] S. E. Wiberley, N. B. Colthup, and L. H. Daly, “Introduction to infrared and Raman Spectroscopy,” *ed. NB Colthup and LH Daly, Academic Press, Inc., San Diego*, 1990.
- [2] D. W. Hahn, “Raman scattering theory,” *Department of Mechanical and Aerospace Engineering, University of Florida*, 2007.
- [3] S. P. Levine, Y. Li-Shi, C. R. Strang, and X. Hong-Kui, “Advantages and disadvantages in the use of Fourier Transform Infrared (FTIR) and filter infrared (FIR) spectrometers for monitoring airborne gases and vapors of industrial hygiene concern,” *Applied Industrial Hygiene*, vol. 4, no. 7, pp. 180–187, 1989.
- [4] C. Aragon, J. A. Aguilera, and F. Penalba, “Improvements in quantitative analysis of steel composition by laser-induced breakdown spectroscopy at atmospheric pressure using an infrared Nd: YAG laser,” *Applied spectroscopy*, vol. 53, no. 10, pp. 1259–1267, 1999.
- [5] S. S. Yin and P. Ruffin, *Fiber optic sensors*. Wiley Online Library, 2002.
- [6] P. F. Bernath, *Spectra of atoms and molecules*. Oxford University Press, 2015.
- [7] W. Slutter and J. Marcovecchio, “Czerny-Turner Monochromator,” *US Patent . . .*, pp. 1–14, 1993.
- [8] K. Liu and F. Yu, “Accurate wavelength calibration method using system parameters for grating spectrometers,” *Optical Engineering*, vol. 52, no. 1, p. 13603, 2013.
- [9] J. E. Johnston, J. B. Kerr, C. T. McElroy, and D. I. Wardle, “Aberration correction in the brewer spectrophotometer,” *Radiation protection dosimetry*, vol. 91, no. 1-3, pp. 133–138, 2000.
- [10] K.-S. Lee, K. P. Thompson, and J. P. Rolland, “Broadband astigmatism-corrected Czerny–Turner spectrometer,” *Optics express*, vol. 18, no. 22, pp. 23378–23384, 2010.

- [11] C. B. Johnson, “Point-spread functions, line-spread functions, and edge-response functions associated with mtf’s of the form $\exp[-(\omega/\omega_c)^n]$,” *Applied optics*, vol. 12, no. 5, pp. 1031–1033, 1973.
- [12] M. Petrou and C. Petrou, *Image processing: the fundamentals*. John Wiley & Sons, 2010.
- [13] K. Matsushima and T. Shimobaba, “Band-limited angular spectrum method for numerical simulation of free-space propagation in far and near fields,” *Optics express*, vol. 17, no. 22, pp. 19662–19673, 2009.
- [14] D. Misra, “Uniform Plane Waves,” *Practical Electromagnetics: From Biomedical . . .*, 2007.
- [15] InPhotonics, “RPB Fiber Optic Raman Probe,” Tech. Rep. 781.
- [16] F. Gillard, Y. Ferrec, N. Guérineau, S. Rommeluère, J. Taboury, and P. Chavel, “Angular acceptance analysis of an infrared focal plane array with a built-in stationary Fourier transform spectrometer,” *JOSA A*, vol. 29, no. 6, pp. 936–944, 2012.
- [17] Hamamatsu, “ORCA-flash4.0 v2,” tech. rep.
- [18] P. K. Girija and A. Prince, “Robustness evaluation of SMO in sensorless control of BLDC motor under DTC scheme,” in *Power Signals Control and Computations (EPSCICON), 2014 International Conference on*, pp. 1–6, IEEE, 2014.
- [19] V. C. Ilioudis and N. I. Margaris, “Sensorless speed and position estimation of PMSM using sliding mode observers in γ - δ reference frame,” in *Control and Automation, 2008 16th Mediterranean Conference on*, pp. 641–646, IEEE, 2008.
- [20] N. R. Lomb, “Least-squares frequency analysis of unequally spaced data,” *Astrophysics and space science*, vol. 39, no. 2, pp. 447–462, 1976.